

TITLE

Joint single cell DNA-Seq and RNA-Seq of gastric cancer reveals subclonal signatures of genomic instability and gene expression

Noemi Andor^{1,†}, Billy T. Lau^{2,†}, Claudia Catalanotti³, Vijay Kumar³, Anuja Sathe¹, Kamila Belhocine³, Tobias D. Wheeler³, Andrew D. Price³, Maengseok Song³, David Stafford³, Zachary Bent³, Laura DeMare³, Lance Hepler³, Susana Jett,³ Bill Kengli Lin³, Shamoni Maheshwari³, Anthony J. Makarewicz³, Mohammad Rahimi³, Sanjam S. Sawhney³, Martin Sauzade³, Joe Shuga³, Katrina Sullivan-Bibee³, Adam Weinstein³, Wei Yang³, Yifeng Yin³, Matthew A. Kubit¹, Jiamin Chen¹, Susan M. Grimes², Carlos Jose Suarez⁵, George A. Poultides⁴, Michael Schnall-Levin³, Rajiv Bharadwaj³, Hanlee P. Ji^{1,2}

† These authors contributed equally to this work.

INSTITUTIONS

¹Division of Oncology, Department of Medicine, Stanford University School of Medicine, Stanford CA, United States

²Stanford Genome Technology Center, Stanford University, Palo Alto CA, United States

³10X Genomics, Pleasanton CA, United States

⁴Department of Surgery, Stanford University School of Medicine, Stanford CA, United States

⁵Department of Pathology, Stanford University School of Medicine, Stanford CA, United States

CORRESPONDING AUTHORS

Hanlee P. Ji

Email: genomics_ji@stanford.edu

Rajiv Bharadwaj

Email: rajiv@10xgenomics.com

ABSTRACT

Sequencing the genomes of individual cancer cells provides the highest resolution of intratumoral heterogeneity. To enable high throughput single cell DNA-Seq across thousands of individual cells per sample, we developed a droplet-based, automated partitioning technology for whole genome sequencing. We applied this approach on a set of gastric cancer cell lines and a primary gastric tumor. In parallel, we conducted a separate single cell RNA-Seq analysis on these same cancers and used copy number to compare results. This joint study, covering thousands of single cell genomes and transcriptomes, revealed extensive cellular diversity based on distinct copy number changes, numerous subclonal populations and in the case of the primary tumor, subclonal gene expression signatures. We found genomic evidence of positive selection – where the percentage of replicating cells per clone is higher than expected – indicating ongoing tumor evolution. Our study demonstrates that joining single cell genomic DNA and transcriptomic features provides novel insights into cancer heterogeneity and biology.

INTRODUCTION

Single cell DNA sequencing (**scDNA-Seq**) identifies somatic genetic alterations such as somatic copy number variants (**CNVs**). For cancer, single cell CNVs paint a high-resolution profile of intratumoral heterogeneity and subclonal structure¹⁻⁴ present in primary tumors^{5,6}, metastases^{7,8}, patient-derived xenografts and even cancer cell lines⁹. This underlying genomic variation seen among a cancer's subclonal populations provides a "fuel" for tumor evolution and adaptation to ongoing therapy. Notably, the dominant subclones of resistant tumors^{5,6}, metastases^{7,8}, patient-derived xenografts and cell lines⁹ often originate from minor subclones in the primary tumor.

The prevalence of intratumoral heterogeneity has implications for cancer biology studies. Cancer cell lines are used to model tumor growth, evaluate metastatic potential and determine drug sensitivities. However, cancer cell lines have subpopulations with extensive fitness diversity^{9,10}. This may lead to different drug responses within the same cell line¹⁰. The application of single cell DNA-Seq quantifies the extent of subclonal diversity that may impact these type of studies.

This scDNA-Seq approach relies on either low coverage whole genome sequencing (**WGS**) to identify somatic CNVs or targeted sequencing to identify cancer mutations^{1-4,11,12}. However, the cellular throughput of scDNA-Seq has been limited, with a typical maximum of hundred cells. Greater sampling of tumor tissues provides an opportunity to expand the scope of intratumoral characterization. However, increasing cellular sequencing throughput is difficult for a number of reasons: limitations of single cell partitioning methods whether plate-based or using flow cytometry isolation⁴; issues with amplifying genomic DNA from single cells; complex methods for isolating nuclei; intricate enzymology steps for library preparation^{13,14}. As a solution that enables massive scale scDNA-Seq, we developed a droplet-based partitioning technology that rapidly processes thousands of cells per sample for library preparation in a highly automated fashion. Using this new approach, we conducted single cell WGS on thousands of cells for nine gastric cancer cell lines and a primary gastric tumor. This extensive cellular

sampling provided robust characterization of subclonal structure of gastric cancer, determined cell cycle assignments and identified quantitative features related to tumor cell selection.

The majority of single cell genomic studies of cancer have focused on the use of single cell RNA-Seq (**scRNA-Seq**), where one sequences thousands of individual transcriptomes from a given tumor^{3,15-17}.

By conducting a joint scDNA-Seq and scRNA-Seq analysis, one identifies underlying genomic alterations among the cells in the sample, subclonal cellular diversity and transcriptome features indicative of differences in biological pathways among the cellular populations. There are only a few studies, such as published by Kim et al.³, which combine both single cell methods for studying cancer^{3,15-18}. Technical challenges limit the number of cells for WGS analysis and conducting joint studies, outside of cancer, often rely on specific large cell types, such as oocytes that are readily manipulated¹⁵.

To conduct a parallel, joint scDNA-Seq and scRNA-Seq study of cancer cells, we also performed a separate, large-scale single cell transcriptome analysis of the same ten cancers (**Fig. 1a**). Analyzing over 30,000 cellular transcriptomes from this set of cancers, we determined CNVs based on scRNA-Seq. Subsequently, we compared the CNV-defined subclonal populations detected from both scRNA-Seq and scDNA-Seq and in the case of the primary gastric tumor, overlaid the data to ascribe transcriptional features to subclonal populations.

RESULTS

High throughput processing for single cell DNA-Seq

For the isolation of large numbers of single cells during library preparation, we developed a two-stage microfluidic droplet-based technology for the automatic generation of high cell number scDNA-Seq libraries. Similar to linked-read sequencing for genome phasing¹⁹ and single cell transcriptome analysis²⁰, microfluidic droplets were loaded with a barcoded hydrogel bead that tags DNA. This

feature enabled the tracking of sequence reads originating from individual droplets and their analyte molecules. In a first microfluidic chip, individual cells were encapsulated with paramagnetic particles and hydrogel matrix precursors to form cell-containing magnetic hydrogel beads, or ‘cell beads’ (**CBs**). As in previous studies that load single cells into microfluidic droplets for transcriptomic studies²⁰, cellular suspensions were first loaded at Poisson limit dilution into droplets using a microfluidic chip. The resultant CBs contained either zero, one or multiple cells (**Fig. 1b,i**).

After breaking the gelled CB emulsion, we used the magnetic properties of the encapsulating cell matrix to efficiently integrate microfluidic and macrofluidic processes to enable nuclear DNA processing for downstream amplification and barcoding. The CB hydrogel structure remains intact after emulsion breaking. The pore structure of the CB matrix facilitated the confinement of large genomic DNA molecules while keeping them diffusively accessible to lysis and denaturation agents. We used this CB feature to lyse cells, digest proteins, and denature DNA. This process yielded freely accessible DNA trapped in CBs suitable for re-partitioning in a second microfluidic step.

In a second microfluidic chip, processed CBs were injected into another microfluidic droplet generator cartridge for barcoding and single-cell whole genome amplification. A novel microfluidic system was employed whereby a single CB is encapsulated alongside a single barcoded gel bead (**GB**) with high efficiency leading to a cell bead-gel bead (**CBGBs**) emulsion (**Fig. 1b,ii**). The barcoded GB was similar to those used in previous studies for phasing genomes¹⁹ and single cell transcriptome profiling²⁰ – an individual GB was functionalized with millions of copies of identical barcoded oligonucleotides that uniquely identifies a droplet during the sequencing reaction. The total number of unique droplet barcodes was approximately 737,000. The CBGB emulsion contained droplets with one, two, or three co-encapsulated beads. Up to 80% of droplets contained two beads consisting of only one CB and only one GB. The remainder consisted of a mixture of doubly loaded barcode GBs, doubly loaded CBs, or droplets loaded with three beads (**Fig. 1b,ii**).

After encapsulation and incubation, the CBGB emulsion was broken and underwent a modified library preparation protocol for Illumina sequencing (**Methods**). Overall, the throughput of this microfluidic-based cellular isolation system demonstrated a scale up to tens of thousands of cells per a microfluidic chip. This processing capacity exceeded flow cytometry-based isolation by several orders of magnitude²⁰. Afterwards, single cell DNA libraries were sequenced with an Illumina system.

Sequencing genome stable diploid cells

For a baseline, we evaluated genome stable diploid cells using peripheral blood mononuclear cells (**PBMCs**). These studies enabled us to determine the extent of amplification bias, genomic dropout, and baseline ploidy calling performance. Data processing is described in the **Methods** section. We filtered aligned sequence reads specific to a single cell. The first 16 base pairs of Read 1 consist of a droplet-identifying barcode sequence. When counting the empirically observed distribution of reads per cell bead barcodes, we observed a strong bimodal distribution where there was a strong enrichment of reads belonging to less than 1% of all observed barcode sequences in the dataset (**Fig. 2a**). To identify droplet barcodes containing a single cell, we filtered outlier read counts and set a reads-per-barcode cutoff extrapolated from the barcode read maxima (**Methods, Fig. 2a**). Approximately 96% of barcoded reads were assignable to a single cell, indicating the minimal spurious DNA contamination or amplification in other droplets.

To evaluate the performance of single cell loading per cell barcode, we analyzed a cellular mixture containing a mixture of human HEK-293T and mouse NIH-3T3 cells. After scDNA-Seq, doublet cells were identified by cellular barcodes with reads aligning to both mouse and human genomes. From a total of 1,313 cells, we observed that less than 2% of cells contained reads belonging to both species (**Fig. 2b**), indicating that the vast majority of cells were loaded as single cells into CB emulsions. This result also indicated our ability to separate distinct cellular genomes.

Overall, we sequenced 1,046 diploid PBMCs with 1.2 billion 2x100 paired-end read pairs. The library had a median read duplication ratio of ~13% per cell, indicating a high overall complexity (**Fig. 2c**). At least 100,000 reads per cell were sequenced, leading to at least one read per every 20kb genomic window (**Supplementary Fig. 1a**). Generating Lorenz curves between the number of reads and fraction of genome sequenced, we determined that coverage demonstrated uniform amplification comparable to another method (**Fig. 2d**)²¹. Finally, we measured the extent of heterogeneity of sequencing characteristics between droplet partitions. As the number of reads per genomic bin is approximately one, we hypothesized that the variation in coverage in a single bin across different cells would follow Poisson statistics. Hence, we plotted the coefficient of variation of each genomic bin's coverage versus its mean. We observed a strong correlation between the coefficient of variation versus the mean as one would expect from a Poisson distribution (**Fig. 2e**).

To determine CNVs for each cell, we modeled per-cell read counts per genomic bin as a Poisson distribution dependent on both the GC content and the copy number (**Methods**). GC bias was modeled as a quadratic function with fixed intercept and correction on a cell-by-cell basis was performed. To estimate copy number for each bin, we empirically computed the effect of GC content (**Supplementary Fig. 1b**) followed by scaling to generate haploid-scaled copy number calls. To identify candidate breakpoints, we calculated the discontinuity in copy number values among all mappable bins using the log-likelihood ratio statistic (**Supplementary Fig. 1c**). Finally, read counts were centered on integer copy number states by numerical optimization to generate haploid-scaled calls. Full algorithmic and software details are available in **Supplementary Information**. The CNV calls were consistent with those produced by Ginkgo¹¹ (**Supplementary Fig. 1d**). CNVs were generally restricted to regions of the genome (88%) where reads could be confidently mapped (**Methods**).

To assess the rate of false positive copy number calls, we calculated the copy number landscape of 1,046 cells of the PBMC control as described previously (**Fig. 2f**). Copy number segments were divided into 20kb bins across the human genome for each cell. On average, less than 1% of 20kb bins in autosomal regions with high alignment score had a copy number other than 2. This result suggested a negligible false positive CNV calling rate. Specifically, aberrant calls occurred in regions of the human genome, which are difficult to align, such as centromeric and telomeric locations (**Supplementary Fig. 1e**).

Determining cell cycle status in cancer cells

We analyzed gastric cancer cell lines to determine replication- and aneuploidy- specific breakpoints as derived from WGS. We analyzed a total of 8,824 single cells from nine different gastric cancer cell lines (**Supplementary Table 1 and 2**). We identified an average of 2,198 breakpoints per sample that were present in more than 1% of cells per cell line. The scDNA-Seq derived copy number and aneuploidy status was confirmed by SNP array analysis and karyotyping of these same cell lines (**Supplementary Fig. 2**). The average ploidy across cells was consistent with that reported by a separate karyotyping of these same cell lines (**Supplementary Fig. 2c**).

Difference in CNV signatures among cells is the result of subclonal populations with distinct copy number signatures or individual variation in cell cycle states. We focused our analysis of intratumoral heterogeneity on the subset of G0/G1 cells, to reduce the contribution of copy number changes attributable to a cell being in S phase (**Fig. 3a**). For classifying cell cycle state we used three features: i) the cell's ploidy, ii) its number of breakpoints and iii) the distance of breakpoints to replication origins²². The proportion of G0/G1 cells ranged from 58% in SNU-16 to 82% in SNU-668 (**Fig. 3b and Supplementary Table 1**). For a subset of the cell lines, we used flow cytometry analysis to generate comparison data of DNA content (**Supplementary Fig. 5a**). The percentage of replicating cells per scDNA-Seq was positively correlated to the percentage of replicating cells per flow cytometry ($r=0.86$,

P=0.063; **Fig. 3c**). The percentage of G0/G1 cells per scDNA-Seq was also proportional to the doubling time of the cell line ($r=0.76$, P= 0.017; **Fig. 3b**). Specifically, an extended duration in G0/G1 was an indicator of slower cell growth.

We used scRNA-Seq to validate our scDNA-Seq's cell cycle assignment. We conducted scRNA-Seq of 28,209 single cells across the same nine gastric cancer cell lines (**Supplementary Table 3**). Differences in passage number between scDNA- and scRNA-Seq experiments were kept to a minimum and the extent of confluence was typically at 80-90% (**Supplementary Table 2**). Activity profiles of multiple cell cycle pathways have been shown to provide robust cell cycle status classification across different cell types²³. For each individual cell, we quantified the activity of 39 cell cycle pathways from the REACTOME database²⁴ and used these results to determine cell cycle state (**Supplementary Table 4**). Pathways were classified into three groups depending on their main activation timing during G0/G1, S, and G2M. We performed hierarchical clustering of cells and classified clusters based on their cells' pathway activity (**Fig. 3d**). The percentages of G0/G1 cells, assigned with scDNA-Seq versus scRNA-Seq were highly correlated ($r=0.73$, P=0.026, **Fig. 3b**).

Subclonal signatures of genomic instability and ongoing selection with scDNA-Seq

We used scDNA-Seq to characterize the underlying subclonal structure of the cell lines. Approximately 95% of the breakpoints identified by scDNA-Seq were found in less than 1% of the G0/G1 population – we ascribed these events to variance related to DNA replication and not representing true cancer CNVs (**Supplementary Table 1**). We used the remaining CNV segments and patterns of genomic instability to identify subclones within the G0/G1 population. Using the CNV features, we calculated the pairwise distances between cells in Hamming space, thus assigning a higher weight to larger genomic segments. We applied a neighbor joining algorithm, BIONJ²⁵, to build a phylogenetic tree of G0/G1 cells (**Methods**). We defined a clone as the largest subtree within which the maximum distance between its cell members was less than 20% of the affected genome (**Fig. 4a**). The relative fraction of

cells assigned to a subclone is referred to as subclone size. To assign S-phase cells to the subclones detected among the G0/G1 population, we determined the cellular similarity with a Pearson correlation. For example, this approach identified four clones within the G0/G1 population of NCI-N87 (**Fig. 4a,b**). The percentage S cells assigned to each of these four subclones were proportional to their respective G0/G1 representation (**Fig. 4a,b**).

Based on our analysis across the gastric cancer cell lines, anywhere from two to 12 subclones were present per a line (**Supplementary Table 5**). Approximately half of the variation in subclones per cell line was attributed to the cell lines' ploidy and/or the duration since the cell line was first established in culture (adjusted $R^2=0.53$; $p=0.044$; **Supplementary Table 6**). Higher ploidy predicted more clones (coefficient = 3.09; $p = 0.054$), while longer time in culture was predictive of fewer clones (coefficient = -0.29; $p = 0.025$). The latter observation is consistent with a recent finding showing that *in vitro* CNV acquisition rate decreases over time, while signatures of proliferation increase, in line with clonal selection of fitter clones⁹.

Shifts in a cancer cell line's subclonal composition have been shown to frequently result from *in vitro* selection, rather than stochastic processes^{9,10}. To quantify *in vitro* selection among the cancer cell lines, we compared the percentage replicating cells per subclone to the percentage G0/G1 cells in that subpopulation. The two cell cycle states had similar proportions for a given subclone, indicating predominance of clonal stasis (Pearson $r = 0.88$; $p < 2e-16$; **Fig. 4c**). We used a hypergeometric distribution to model the subclone's number of replicating cells and test if it was within a range consistent with its G0/G1 representation (**Methods**). Seventeen subclones (30%) had a higher percentage of replicating cells than expected from their G0/G1 population size (FDR adjusted $P\leq 0.05$; **Fig. 4c,d**). We interpreted this result to be a possible indication of positive selection. Conversely, six subclones (11%) had fewer replicating cells than expected from their G0/G1 representation, suggesting they were under negative selection (FDR adjusted $P\leq 0.05$; **Fig. 4c,d**).

We found that negatively selected subclones were enriched for a CNV gain of *CNOT1* – a gene involved in mRNA degradation (**Fig. 4e**), and for deletions of *IREB2*, *SIN3A* and *MAP2K1* ($|r| \geq 0.32$; $p \leq 0.05$). The overrepresentation of positively selected clones compared to negatively selected ones was consistent with a recent study showing that *in vitro* evolution is primarily driven by positive selection¹⁰. Quantifying the selection of individual subclones may prove useful in predicting the genome states of future cell line populations.

Consilience of scDNA- and scRNA-Seq on G0/G1 subclonal architectures

As per this study, scDNA-Seq provides high resolution analysis of CNVs than single cell gene expression studies. However, the use of joint sets offered a way of determining comparison of clonal overlap. First, we determined whether scRNA-Seq identified the same set of subclones derived from scDNA-Seq. For this comparison, we inferred CNVs from scRNA-Seq. Gene expression has been shown to be proportional to the gene's copy number state for the majority of genes²⁶, suggesting that scRNA-Seq derived expression features can inform CNV status. However, other mechanisms of gene regulation alter expression, confounding the influence of segmental copy number. This is most evident when analyzing short genomic segments, below 10 Mb. One algorithm for calling CNVs from scRNA-Seq data demonstrated good performance, particularly for large segments, above 10 Mb, and for large subclones²⁷. However, this method's precision fell below 50% for smaller subclones, making up 20% or less of the total cells²⁷. To address this issue, we developed and applied an algorithm called LIAYSON, which uses scRNA-Seq to deconvolute bulk CNV profiles into single cell specific copy numbers (**Methods**). This approach relies on gene expression to estimate the variance in copy number, but not the mean copy number across cells (**Supplementary Fig. 3a,b**), and is therefore less influenced by regulators of expression levels other than CNVs. It requires on average at least 20 genes with expression results from a genomic interval of at least 10 Mb. Between 25-80% of segments per cell line passed these metrics for this analysis.

With the CNV results from scRNA-Seq, we identified a range of three to 11 subclonal populations across the nine gastric cancer cell lines (**Supplementary Table 5**). The number of scRNA-Seq and scDNA-Seq derived clones were highly correlated ($r=0.93$. $P=3E-4$; **Fig. 5a**). As another validation of concordance between the two methods, we performed hierarchical clustering of subclone-specific CNV profiles (**Fig. 5b-d**). We defined true positives as clusters containing subclones identified by both methods and discordance for clusters containing only one type of subclones but not the other (**Methods**). The concordance between scDNA-Seq and scRNA-Seq had an average F1 score of only 0.47 for clones below 4% abundance, but increased to ≥ 0.7 for clones above 4% size (**Supplementary Fig. 3c**). Based on this result, we excluded any subclones smaller than 4% size and not confirmed by both single cell methods. Posteriori saturation curves of scDNA-Seq library sizes were calculated for each cell line as previously described² and indicated that we had statistical power to detect these subclones (**Supplementary Table 7**).

Citing an example, our scDNA-Seq and scRNA-Seq results identified four subclones in NCI-N87 with similar proportional sizes (**Fig. 5b-d**). On closer examination we observed that the copy number states of several smaller segments (<10 Mb), were not assigned for any clone by scRNA-Seq, but were identified by scDNA-Seq. For these genomic regions, the number of genes with adequate expression levels was too low to allow assignment by scRNA-Seq (**Fig. 5e**). Therefore, our conclusion was that scDNA-Seq provided higher degree of subclonal characterization.

The other gastric cancer cell lines had similar results. Among the nine cell lines, the subclonal size, as determined by scRNA-Seq, correlated with the scDNA-Seq results (Pearson $r=0.93$, $p < 2e-16$; **Supplementary Fig. 3d**). An average of 88% cells per cell line were assigned to subclones confirmed by both scDNA-Seq and scRNA-Seq (**Supplementary Table 5**). The discordance was attributable to subclones with a 10% or lower cellular fraction. Concordance between the two methods was

dependent on the sequence depth, the subclone size (**Supplementary Fig. 3c-f**) and the subclonal number per a given cell line (**Supplementary Table 5**). For SNU-16 and SNU-668, differences in passage number between scDNA- and scRNA-Seq experiments were correlated with a greater divergence between clonal compositions measured by the two methods ($r=0.71$, $P=0.032$; **Supplementary Fig. 3g**). Thus, CNV comparisons enable clonal overlaying with scDNA-Seq providing higher resolution of subclonal genomic characteristics.

Analyzing a primary gastric cancer with joint single cell sequencing

As a test of joint single cell genomics on a clinical tissue sample, we analyzed a Stage II gastric adenocarcinoma (**P5931**). We determined CNVs, gene expression, subclonal assignment and pathway activity for a given single cell. Histopathology of this gastric cancer revealed moderate to poorly differentiated features with a 60-70% tumor fraction. Immunohistochemistry demonstrated a loss of *MLH1* and *PMS2* expression. The loss of these proteins indicated that this tumor had microsatellite instability (**MSI**) where cancer cells have a hypermutable state because of loss of DNA mismatch repair. The tumor tissue was disaggregated into a single cell suspension and analyzed with both single cell genomic methods (**Methods**).

From this patient-derived tumor sample, we sequenced 796 cells using scDNA-Seq and 2,098 cells using scRNA-Seq. The G0/G1 representation was 79.5% among scDNA- and 61% among scRNA-sequenced cells (**Supplementary Fig. 4a,b**). After eliminating cell-cycle related breakpoints (**Supplementary Fig. 4a**), a total of 28 CNVs were identified among the G0/G1 population, including gain of chromosome 8, 3 and 19q - three of the four allelic imbalances are among the most common events in MSI-positive gastric cancers²⁸. Both scDNA-Seq and scRNA-Seq identified four clones (**Fig. 6a**) with three being concordant and making up over 90% of the cells in each assay. A diploid subpopulation comprised 59% of the scDNA- and 50% of the scRNA-sequenced G0/G1 population (**Fig. 6a**).

The scRNA-Seq results provided transcriptional features for each subclonal population. Consistent with immunohistochemistry, *MLH1* expression was mostly absent, but *PMS2* expression was low to moderate (detected in 1.6% and 16.5% of G0/G1 cells respectively). To distinguish the non-epithelial population from epithelial, we used differences in the epithelial marker *EPCAM*. In contrast to *EPCAM-* cells (27% of the G0/G1 population), which were diploid, the majority of *EPCAM+* cells harbored CNVs (**Fig. 5b,c**). Thus, most of the epithelial cells were cancer, while most diploid cells were non-epithelial. After excluding the myofibroblasts/fibroblasts (13%), endothelial cells (1.6%) and immune cells (12.3%) (**Fig. 5d,e**), the normal, diploid cells comprised 47% of the epithelial population. Differences in the activities of canonical pathways among the various epithelial cellular subpopulations (i.e. tumor, normal) were calculated with Gene Set Variation Analysis (**GSVA**) as noted in the **Methods**. Differences among the activities of canonical pathways among tumor clones as well as between tumor clones and the normal subpopulation were evident. The top pathway functions enriched in the tumor epithelial cells included upregulation of genes involved in epidermal growth factor receptor (**EGFR**) signaling (**Fig. 6f and Supplementary Table 8**).

On close examination, differential pathway activities were apparent when comparing two subclones (**Fig. 6a**). The smaller one had higher Rac activation and the activity of the citric acid cycle was increased suggesting higher metabolic activity (**Fig. 6f**). In contrast, pathways indicating Notch signaling, nuclear envelope formation and reassembly and PECAM1 interactions – shown to play a role in conferring pro-angiogenic properties to endothelial cells – had a higher transcriptional levels in the larger tumor subclone (**Fig. 6f**). Overall, examining the transcriptional signatures of a given subclone delineates different phenotypes indicative of biological divergence.

DISCUSSION

For this study we demonstrated a new scDNA-Seq technology that enabled the interrogation of intratumoral heterogeneity from thousands of cells per sample. We also demonstrated how a joint analysis, adding RNA-Seq at the resolution of single cells, provided new types of information about cancer evolution in the context of cellular heterogeneity. To compare scDNA-Seq and scRNA-Seq derived clones, we developed a new method that leveraged association-rule mining to infer large-scale CNVs from scRNA-Seq. Co-clustering clones identified by either single cell method intrinsically controlled for false positives: whether two clones co-cluster not only depends on their own genetic content, but also on the content of other clones identified in the sample. Integrating the transcriptome and genome features allowed us to characterize the genetic basis of clonal expansions and identify seminal features of underlying pathway dysregulation across diverse clonal populations. Subsequently, we demonstrated that this analysis utility on primary tumor biopsies.

Our study showed that gastric cancer cell lines have substantial genetic subclonal diversity. This result is consistent with other studies showing that cancer evolution continues *in vitro*^{9,29}. Cell line heterogeneity has implications for *in vitro* drug studies where the clonal composition may prove to be an important factor. Moreover, one can use cell lines for *in vitro* studies of clonal competition, therapeutic adaptation and transcriptional reprogramming³. Cellular diversity in cancer cell lines can be the result of stochastic drift or of ongoing selection. Several approaches have been developed to quantify selection using either time-resolved sequence data from longitudinal studies^{30,31} or by observing differences in the statistical structure and shape of genealogies reconstructed from a fitness diverse asexual population^{32,33}. Our integrated sequencing approach enabled prediction of selection strength by simply comparing S to G0/G1 representations of a clone. Our study also showed results consistent with a significant proportion of subclones undergoing both positive and negative selection. This result is consistent with prior observations that cancer cell line diversification is a consequence of

in-vitro selection¹⁰. For future studies, we will use joint single cell analysis for both translational studies of clinical tumor samples as well as *in-vitro* studies to relate a cell's level of genomic instability to its fitness relative to cancer therapy.

Accession codes. Data have been deposited in dbGAP under accession number phs001711.

ACKNOWLEDGEMENTS

This work was supported by the following grants from the NIH: NHGRI g to S.M.G. and H.P.J. and NCI U01CA217875 to A.S. and H.P.J. The American Cancer Society provided additional support to J.C. and H.P.J. [Research Scholar Grant, RSG-13-297-01-TBG]. In addition, H.P.J. received support from the Clayville Foundation, the Gastric Cancer Foundation and the Seiler Family Foundation. We thank Dino Valdecanas for assistance with chip drafting and Minji Kim for assistance with chip development. Also, we thank Michelle Luo and Steven Short for reviewing the manuscript.

AUTHOR CONTRIBUTIONS

N.A., B.T.L., A.J. C.C., V.K., K.B., T.D.W., A.D.P., M.S., R.B. and H.P.J. contributed to the experimental design. C.C., V.K., K.B., T.D.W., A.D.P., M.S., Z.B., B.K.L., A.J.M., M.R., S.S.S., M.S., J.S., K.S., A.W., W.Y., Y.Y., B.T.L., M.S-L., R.B. contributed to the technology development. B.T.L., A.S., J.C., C.C., M.A.K., T.D.W., A.D.P., M.S., L.D., S.J., B.K.L., A.J.M., M.R., S.S.S., M.S., J.S., K.S., A.W., W.Y. and Y.Y. conducted the experiments. V.K., D.S., L.H., N.A. and B.T.L contributed to the software development. N.A., B.T.L., C.C., V.K., K.B., S.M.G., T.D.W., A.D.P., M.S., L.H., S.M., M.S-L., R.B. and H.P.J. contributed to the data analysis. C.K.S., G.A.P. and H.P.J. contributed to the clinical sample analysis. N.A., B.T.L., V.K. and H.P.J. did the writing. R.B. oversaw the technology development and CNV calling software. H.P.J. oversaw all aspects of the genomics studies.

COMPETING FINANCIAL INTERESTS

The following authors are employees of 10X Genomics: C.C., V.K., K.B., T.D.W., A.D.P., M.S., D.S., Z.B., L.D., L.H., S.J., B.K.L., S.M., A.J.M., M.R., S.S.S., M.S., J.S., K.S-B., A.W., W.Y., Y.Y., M.S-L. and R.B.

FIGURE LEGENDS

Figure 1. Single cell sequencing strategy. (a) Study design. Aliquots of cell suspension were used to conduct separate scRNA-Seq and scDNA-Seq analysis. CNVs are called independently from scDNA- and scRNA-Seq results and used to identify and mutually validate coexisting clones within each sample. ScRNA-Seq informs what genes each clone expresses, while scDNA-Seq has a higher resolution on the genomic instability of each clone. (b) Single cell DNA sequencing technology overview. (i) Cell beads (CBs) are generated by injection of cells into a microfluidic chip with a polymer matrix. Sub-nanoliter droplets are formed, with droplets containing either zero or one cell. After removal of droplets from the microfluidic cartridge, the cell beads form a crosslinked hydrogel bead. After emulsion breaking, the hydrogel CBs remain intact. Lysis and buffer exchange are performed without loss of cellular genomic material. (ii) CBs are loaded alongside barcode-containing gel beads (GBs), which enables the identification of sequence data to the originating droplet partition. Sub-nanoliter droplets are generated containing one of each type of bead. Whole genome amplification and barcoding subsequently takes place, which results in barcode-tagged amplified genomic DNA. The emulsion is then broken and standard library preparation procedures are performed to generate an Illumina sequencing library.

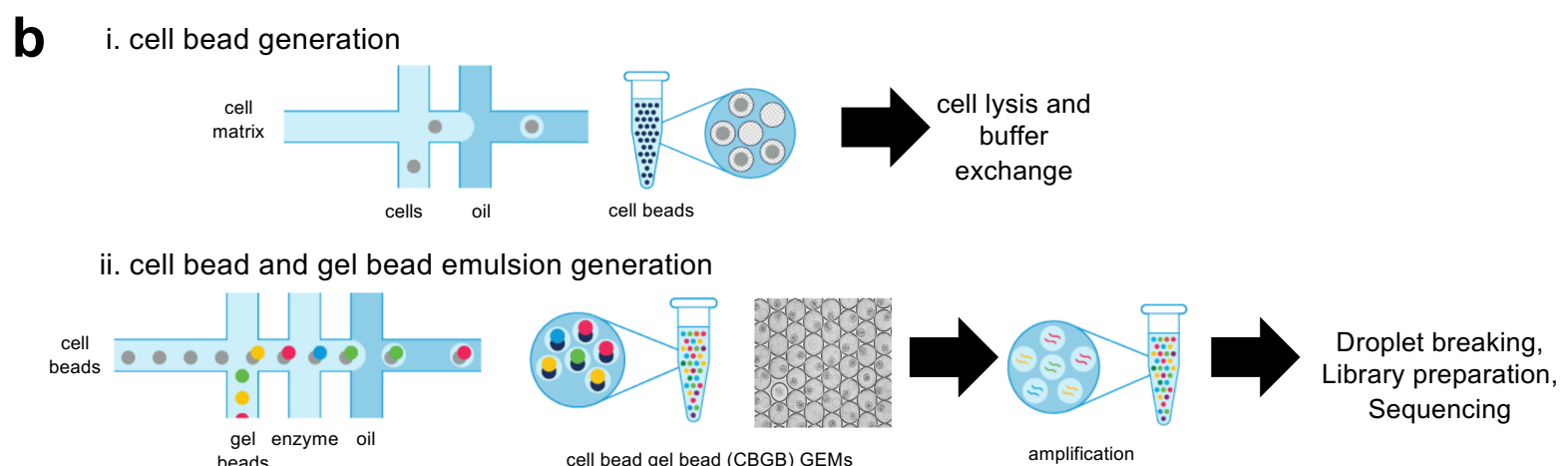
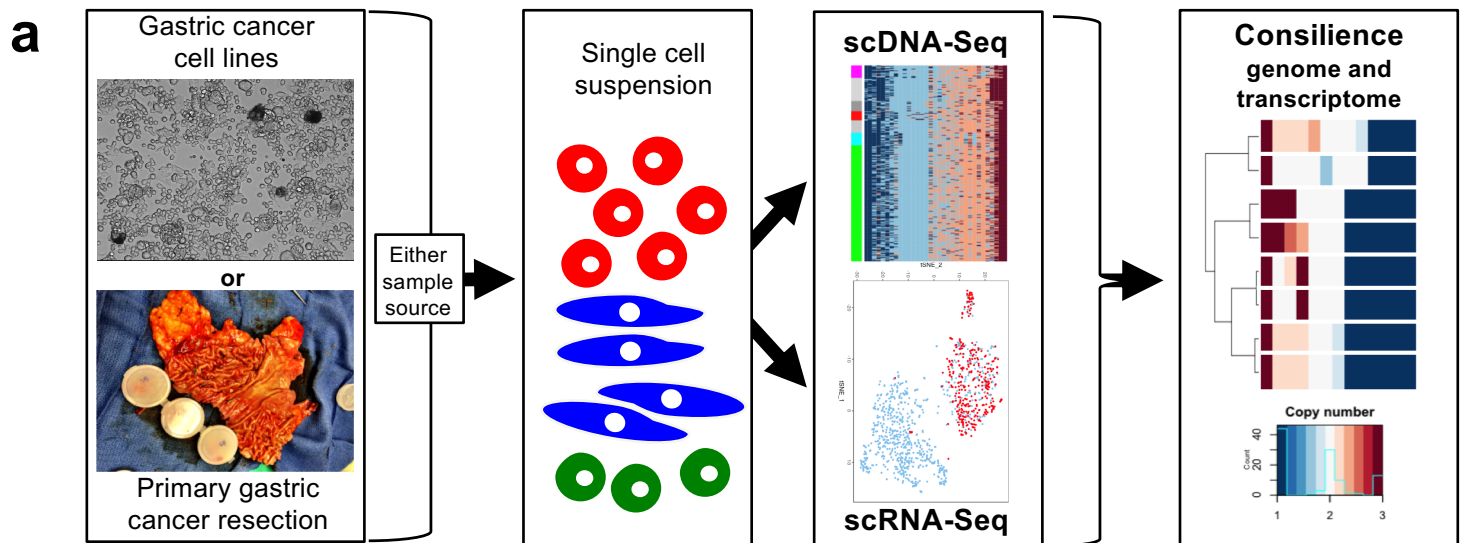


Figure 1

Figure 2. Technical performance of single cell DNA sequencing. (a) Sequence read distribution across droplet barcodes. Barcodes are assigned to be containing a cell based on measuring the quantiles of reads per observed barcode. Cell-containing barcodes are marked as a green line, and make up 96% of all sequence data. (b) scDNA-Seq of cell line mixtures. A mixture of human and mouse cell lines was used to generate a scDNA-Seq library. Each point represents a droplet partition. Black: droplet barcodes determined to be belonging to either only human or mouse genomes. Red: droplet barcodes with reads aligning to greater than 1% of both human and mouse genomes. (c) Unique reads in cell-containing barcodes. A scatterplot of the number of unique reads per barcode versus the fraction of unique reads per barcode is shown. Green points denote barcodes identified as those containing a cell. Dashed line: the cutoff read count for a barcode to be classified as being associated with a cell. (d) Uniformity of scDNA-Seq data. Lorenz curves of 20 PBMC cells selected at random. Curves significantly deviating from the diagonal reflect non-uniformity of amplification. (e) Reproducibility of scDNA-Seq across cells. Each point represents a genomic bin. The coefficient of variation of each genomic bin is plotted against its mean coverage across cells. A high dispersion would indicate significant reaction heterogeneity. (f) Histogram of copy number calls across 20kb bins in GRCh38. Copy number calls in 1,046 PBMCs were grouped according to either the autosomal or sex chromosomal regions.

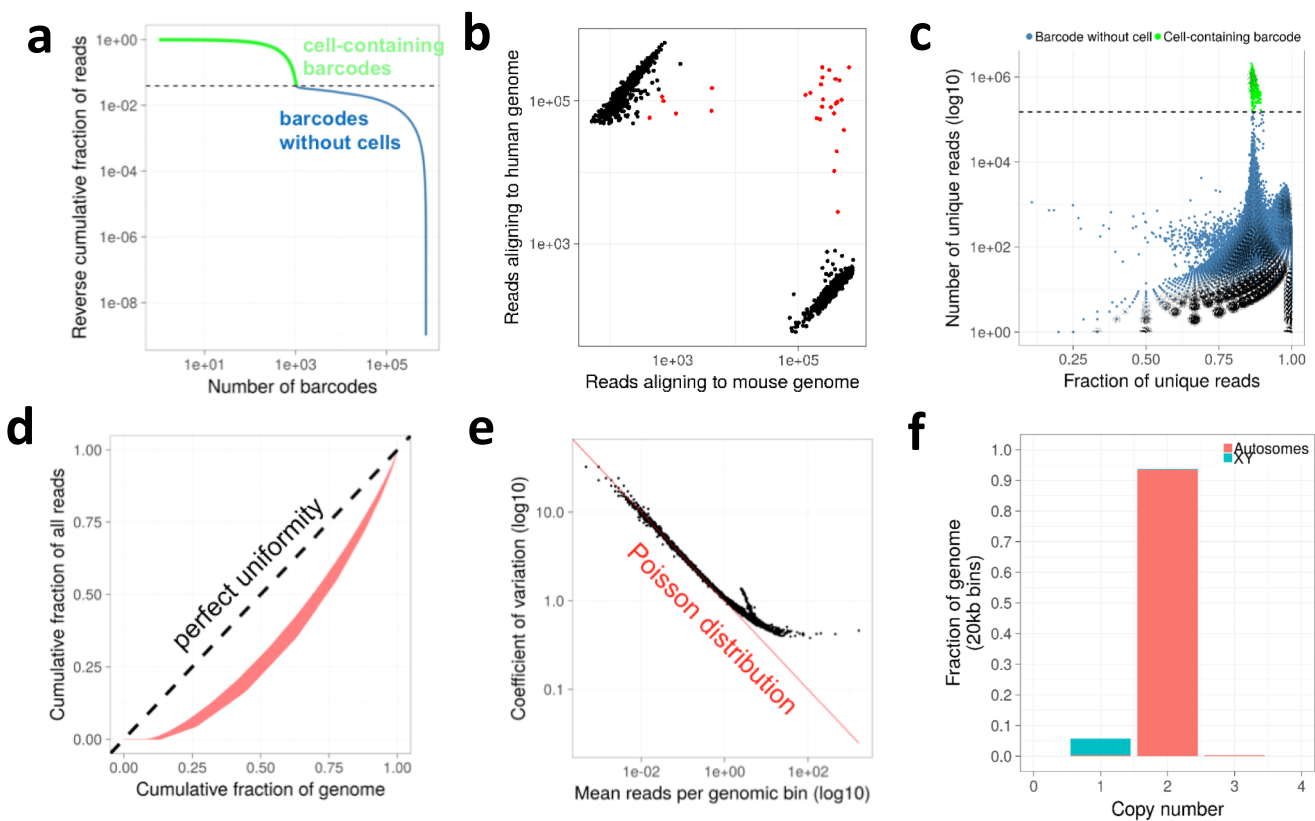


Figure 2

Figure 3. ScDNA- and scRNA-Seq delineate cell cycle state heterogeneity of gastric cancer cell lines. (a-c) scDNA-Seq derived cell cycle assignment. **(a)** 1,005 scDNA sequenced NCI-N87 cells are classified according to three features: their ploidy (x-axis), the number of breakpoints in their genome (y-axis) and their breakpoint's proximity to human replication origins per chromosome (ORIs; color bar). Each cell's uncommon breakpoints (i.e. breakpoints identified in $\leq 1\%$ cells) are counted for each chromosome. For S-phase cells, these counts are correlated to the number of ORIs per chromosome. In contrast to S cells, G0/G1 cells have fewer breakpoints and their count is not correlated to chromosomal ORI counts. **(b)** % G0/G1 cells (y-axis) estimated from scDNA-Seq or scRNA-Seq is positively correlated with doubling time entries. **(c)** Validation of scDNA-Seq informed cell cycle phase assignment with flow cytometry. Cell lines shown were quantified by both techniques from the exact same suspension. **(d)** Cell cycle phase assignment of scRNA sequenced cells. 3,246 NCI-N87 cells (columns) are clustered according to the activity of 39 pathways related to various states along the cell cycle (rows). Clusters are then classified as G0/G1 cells (black), cell in S-phase (cyan) or cells in G2M (red).

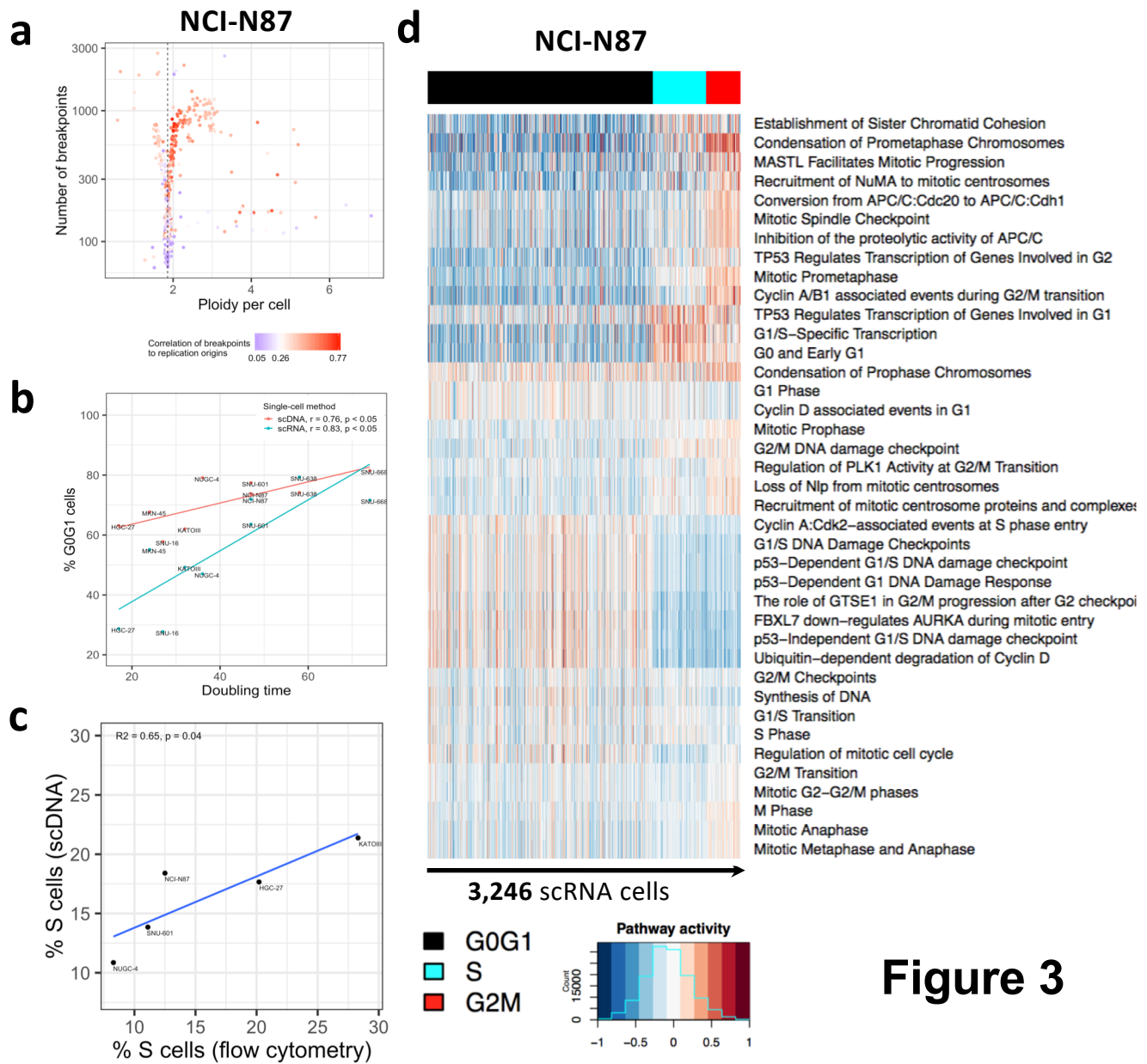


Figure 3

Figure 4: Intra-tumor heterogeneity and evolution in gastric cancer cell lines. (a) Copy number landscape of G0/G1 cells (left) is shown alongside S cells (right) for each clone detected in NCI-N87 (left color bars). **(b)** Copy number segmentation profile shown for a G0/G1- and an S representative of the two largest clones in (a) (cyan and purple). Arrows indicate genomic regions where the two clones diverge. **(c)** % Replicating cells per clone increases with % G0/G1 cells per clone in NCI-N87 as well as in the other eight cell lines, indicating clonal stasis (Pearson $r = 0.88$; $p < 2e-16$). Selection of clones (color-coded) calculated as probability of sampling the % replicating cells observed for a given clone, conditional on the G0/G1 representation of that same clone using the hypergeometric distribution (**Methods**). Clones are assigned to three groups: positive selection ($n=17$), no selection ($n=34$) and negative selection ($n=6$). **(d)** Number of selected clones per cell line. **(e)** Copy number of mRNA deadenylase *CNOT1* relative to baseline ploidy (y-axis) is higher among clones with lower selection coefficients (x-axis). Selection coefficient calculated by subtracting the % G0G1 cells from the % S cells assigned to a clone.

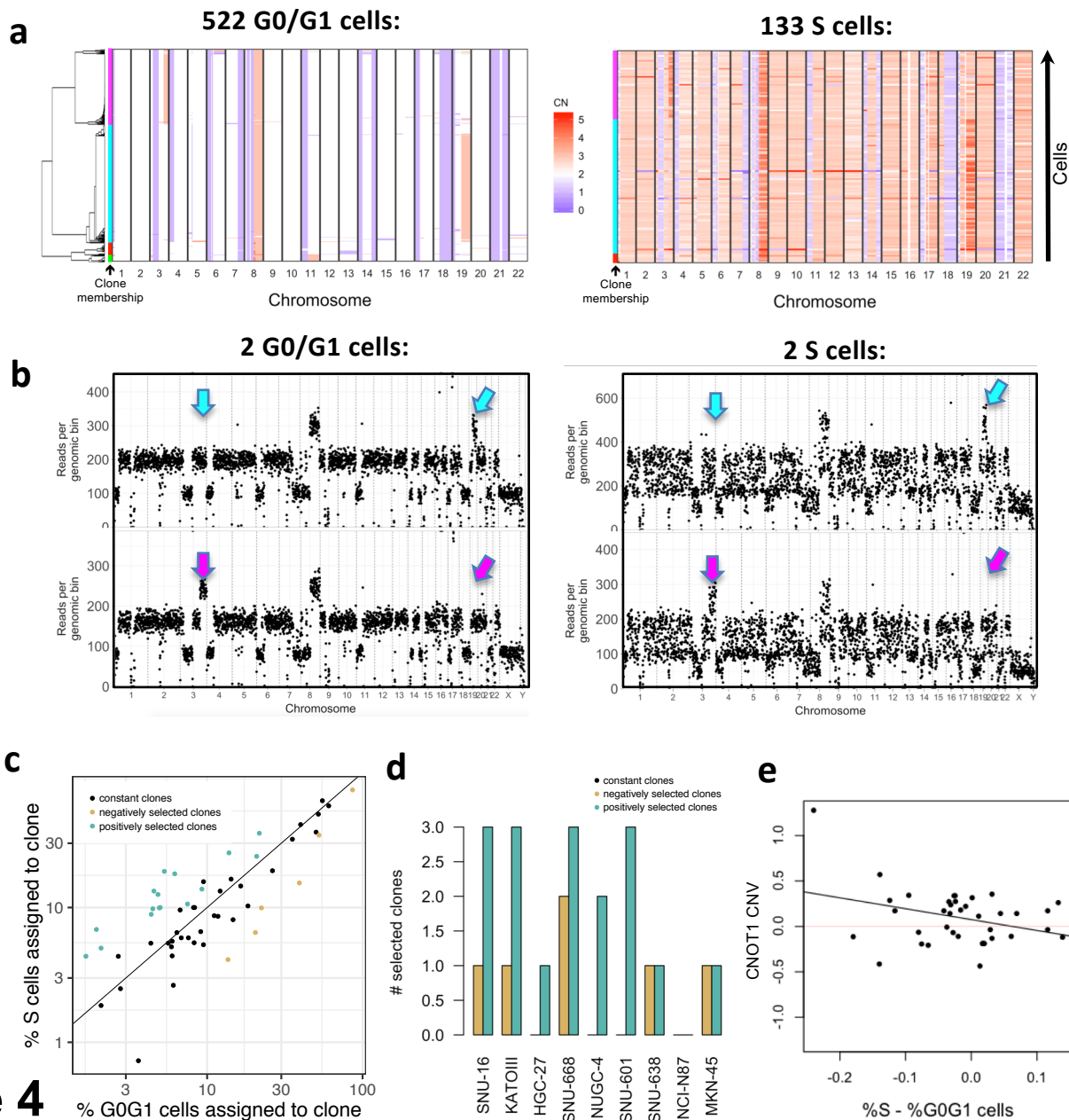


Figure 4

Figure 5: Consilience of scDNA- and scRNA-Seq on G0/G1 clonal architectures. (a) Correlation between number of clones inferred by scRNA- and scDNA-Seq. **(b)** ScDNA-Seq derived copy number landscape (columns) of 742 G0/G1 cells (rows) distinguishes four clones. Clone membership is color coded on the left. **(c)** scRNA-Seq derived copy number landscape of 2,334 G0/G1 cells independently distinguishes four clones (left color bar). **(d)** Each CNV profile found by scRNA-Seq has an equivalent CNV profile in the scDNA-Seq data, applying to a similar % of cells. **(e)** Clone specific differences in CNVs are shown for the two largest NCI-N87 clones (purple and cyan) along with affected cancer genes in those regions. Gray bands are genomic regions too small to be assigned clone-specific CNVs by scRNA-Seq and thus detectable only with scDNA-Seq.

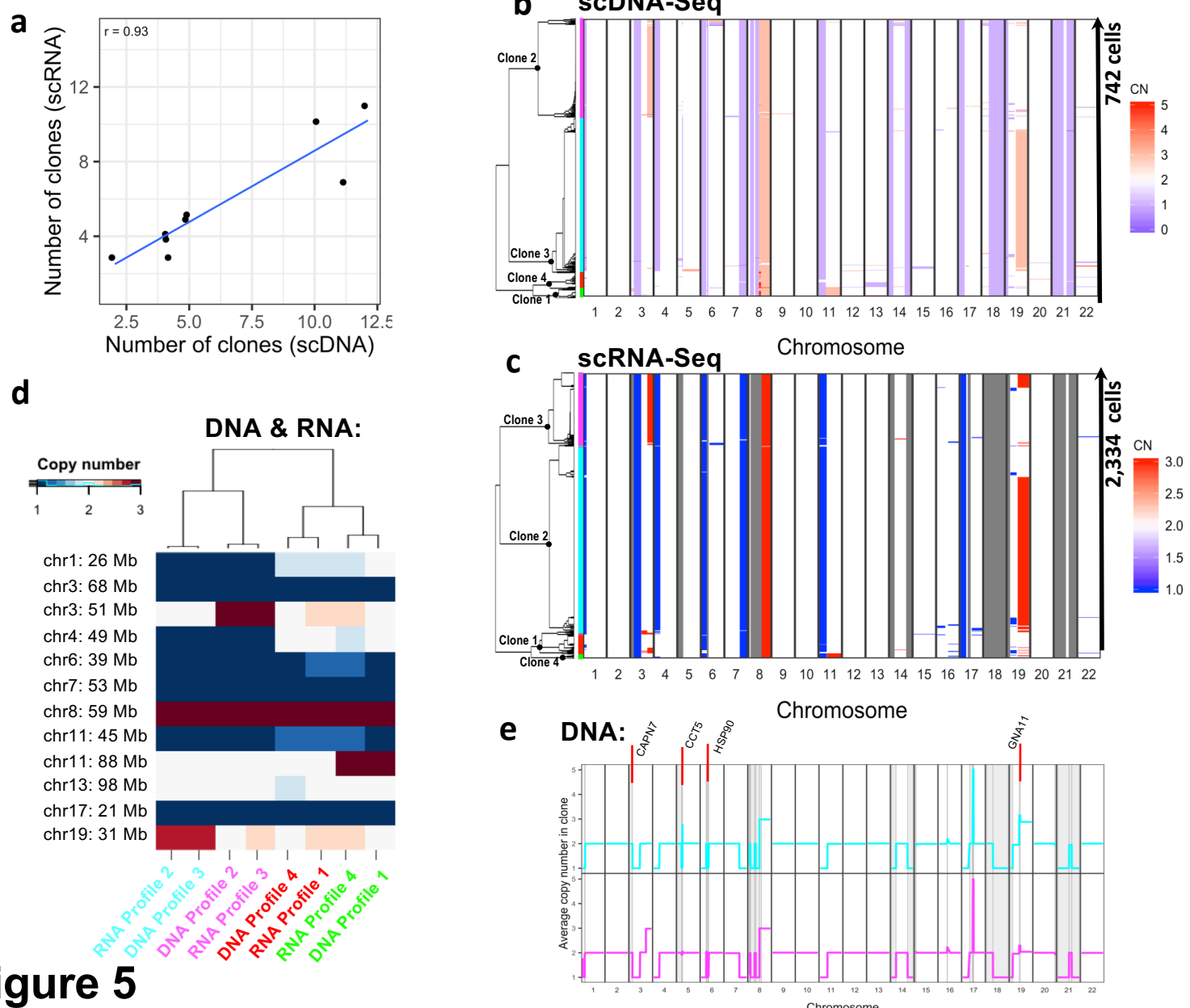
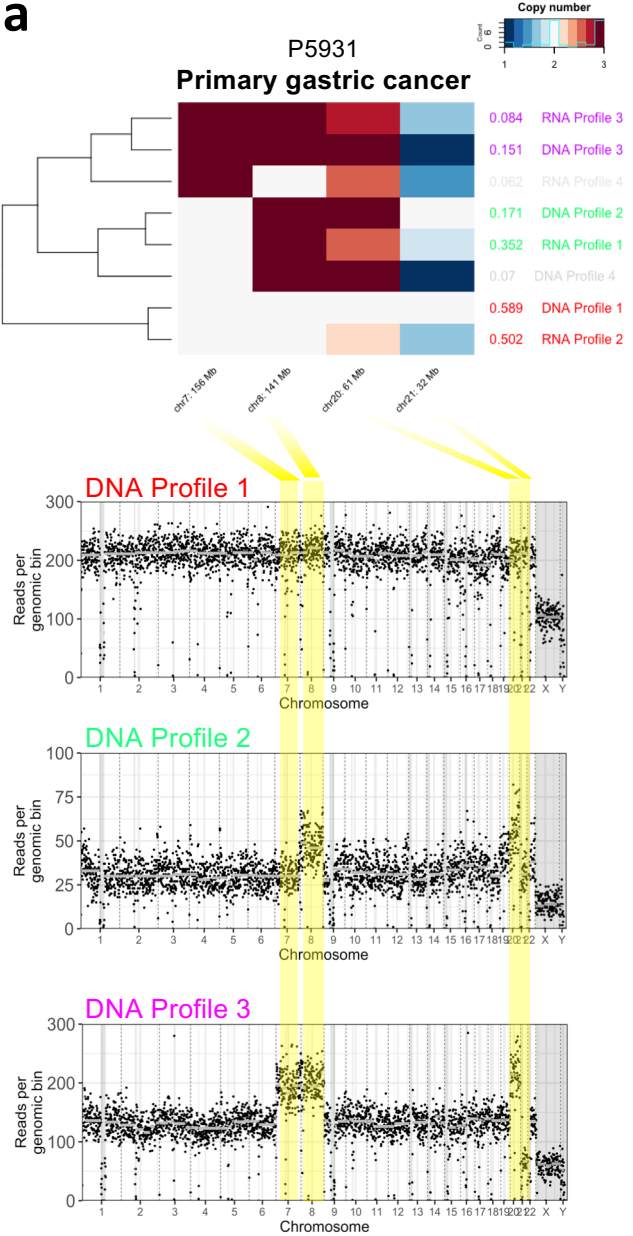


Figure 5

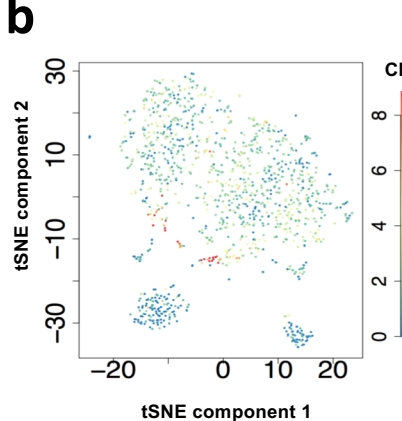
Figure 6. Integrated scDNA- and scRNA-Seq analysis of patient 5931's G0/G1 population. (a)

Both scRNA- and scDNA-Seq independently identify four clones in P5931, each with a distinct CNV profile. Three out of four CNV profiles found by scRNA-Seq have an equivalent CNV profile in the scDNA-Seq data, applying to a similar % of cells. Clone membership is color-coded on the right (gray – identified by either scDNA-Seq or scRNA-Seq alone; rainbow – confirmed by both techniques). Copy number segmentation profiles are shown for three cell representatives – one for each of the three confirmed clones. Yellow bands indicate genomic regions where the clones diverge. **(b-e)** TSNE map of 1,090 G0/G1 cells calculated based on the expression of variable genes (**Methods**). Non-epithelial cells are marked by absence of CNVs **(b)** and of *EPCAM* expression **(c)**, and include myofibroblasts – identified by THY1 **(d)**, and immune cells – identified by higher levels of PTPRC expression **(e)**. **(f)** Differential activation of pathways among clones (Anova: $P < 0.001$).

a



b



c

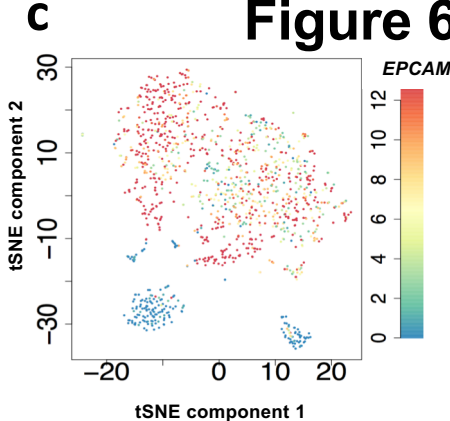
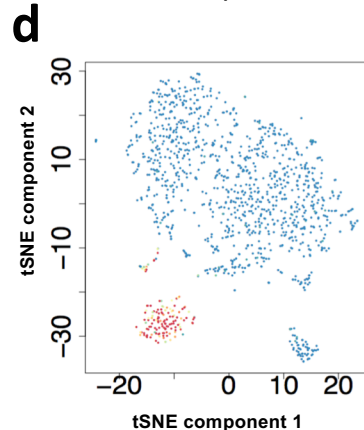
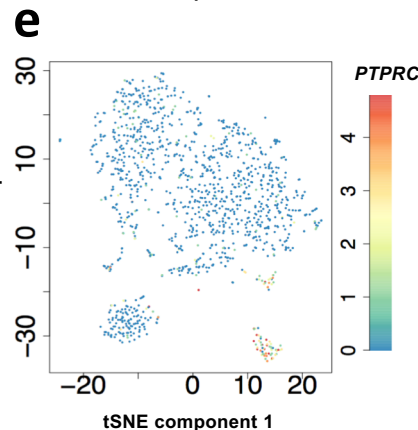


Figure 6

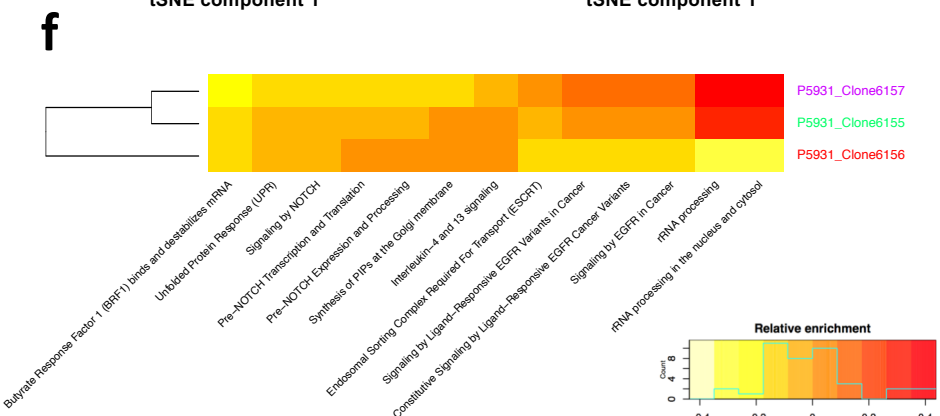
d



e



f



METHODS

Cell lines and gastric cancer patient sample

Gastric cancer cell lines were purchased from ATCC (KATOIII, NCI-N87, SNU-16), KCLB (SNU-668, SNU-601, SNU-638), JCRB (MKN-45, NUGC-4) and ECACC (HGC-27). Cells were cultured in their recommended media conditions at 37°C. Cultured cells were processed into suspensions with standard procedures. Briefly, the cancer cell lines were trypsinized, followed by inactivation by FBS. We performed washes by centrifugation at 400g in 1X PBS with 0.04% BSA. To remove cellular debris and cellular aggregates, we filtered cells through a Flowmi cell strainer (Wayne, NJ) before proceeding to single-cell DNA and RNA sequencing.

For analysis of clinical tumor samples, our study was approved by the Institutional Review Board (IRB) at Stanford University. Informed consent was obtained from the patient. Tissue biopsies were obtained from surgical resection of a primary gastric adenocarcinoma and matched adjacent normal tissue. Immediately after resection, the tumor sample was stored in RPMI medium on ice for less than 1 hour. The sample was then macrodissected and dissociated into a cellular suspension by the gentleMACS Octo Dissociator using the human tumor dissociation kit as per manufacturer's recommendations and the 37C_h_TDK_3 program (Miltenyi Biotec, Bergisch Gladbach, Germany). The suspension was used immediately for scRNA-seq. Single cell DNA-seq was performed after thawing cryopreserved sample stored in liquid nitrogen in 90% FBS-10% DMSO freezing medium.

Library preparation protocol for scDNA-Seq

Single-cell DNA libraries were generated using a high-throughput, droplet-based reagent delivery system using a two-stage microfluidic procedure. First, cells were encapsulated in a hydrogel matrix and treated to lyse and unpackage DNA. Second, a gel bead (GB) was functionalized with copies of a unique droplet-identifying barcode (sampled from a pool of ~737,000) and co-encapsulated with the

hydrogel cell bead in a second microfluidic stage to separately index the genomic DNA (gDNA) of each individual cell. Unless otherwise stated, all reagents were part of a beta version of the Gel Bead and Library Kit for single cell CNV analysis (10X Genomics Inc., Pleasanton, CA).

In the first microfluidic chip, cell beads (**CBs**) were generated by partitioning approximately 10,000 cells of each sample in a hydrogel matrix. A cell suspension is combined with an activation reagent, hydrogel precursors, paramagnetic particles, and loaded into one inlet well. In the other two inlet wells, CB polymer reagent and partitioning oil were added (**Fig. 1b,i**). To ensure a low multiplet rate, cells were delivered at a dilution such that the majority of CBs contain either a single cell or no cell. Once generated, the emulsion was immediately transferred into a PCR strip tube and incubated with orbital shaking at 1000 rpm overnight. The incubation yields polymerized magnetic CBs for subsequent steps.

Encapsulated cells were processed by the addition of lysis and protein digestion reagents to yield accessible DNA for whole-genome amplification. The presence of magnetic particles in the cell bead matrix enabled CB retention and streamlined washing and buffer exchange steps. After lysis, CBs were washed by magnetic capture, concentrated by reduction of liquid volume, and buffer exchanged with the addition of 1X PBS buffer. CBs were then denatured by NaOH, neutralized with Tris, and diluted in storage buffer. Finally, aggregates of cell beads were removed by filtration through a Flowmi strainer before a volume normalization procedure to set the CB concentration.

Cell bead-gel bead (**CBGBs**) were generated by loading CBs, barcoded gel beads, enzymatic reaction mix, and partitioning oil in a second microfluidic chip (**Fig. 1b,ii**). A majority of the **CBGBs** (~80%) contained a single CB and a single gel bead, which once encapsulated then dissolved to release their contents. To amplify and barcode gDNA, the emulsion was then incubated at 30°C for 3 hours, 16°C for

5 hours, and finally heat inactivated at 65°C for 10 minutes before a 4°C hold step. This two-step isothermal incubation yielded genomic DNA fragments tagged with an Illumina read 1 adapter followed by a partition-identifying 16bp barcode sequence.

The emulsion was broken and purified as previously described¹. Conventional end-repair and a-tailing of the amplified library was performed, after which a single-end sequencing adapter containing the Illumina read 2 priming site was ligated. PCR was performed using the Illumina P5 sequence and a sample barcode with the following conditions: 98°C for 45 seconds, followed by 12-14 cycles (dependent on cell loading) of 98°C for 20 seconds, 54°C for 30 seconds, and 72°C for 30 seconds. A final incubation step at 72°C was performed for 1 minute before holding at 4°C. Libraries were purified with SPRIselect beads (Beckman Coulter, Brea, CA) and size-selected to ~550bp. Finally, sequencing libraries were quantified by qPCR before sequencing on the Illumina platform using NovaSeq S2 chemistry with 2x100 paired-end reads.

ScDNA-Seq data processing and CNV calling

Sequencing data was processed with the Cellranger-dna pipeline, which automates sample demultiplexing, read alignment, CNV calling, and report generation. In this study, we used a beta version for all analyses (6002.16.0). Paired-end FASTQ files and a reference genome (GRCh38) are used as input. Cellranger-dna output includes copy number calls for each cell.

The computational pipeline includes **preprocessing** and **single cell copy number calling**. The outputs of this pipeline are CNV calls and read counts in 20kb bins across the genome as genomic bin-by-cell matrices. A summary is provided in this section - full details are included in the **Supplementary Material**. In the preprocessing stage, the first 16 base pairs of read 1 are compared to a whitelist of all possible droplet barcodes (totaling ~737,000). All observed droplet barcodes were tested for the

presence of a cell by using mapped read abundances to the human genome. Reads were aligned to GRCh38 using bwa-mem. Each read in the bam file was annotated with a cellular barcode tag ‘CB’. Confidently mapped reads were counted across the genome in 20kb non-overlapping windows. GC bias correction, modelled as a polynomial of degree 2 with fixed intercept, was applied. Copy number calls are determined by modeling binned read abundances to a Poisson distribution with the copy number, GC bias, and a scaling factor as parameters. Candidate breakpoints were estimated by applying a log-likelihood ratio statistic against fluctuations in read coverage over neighboring genomic bins. These breakpoints were refined and reported as a set of non-overlapping segments across the genome. The copy numbers were scaled to integer-level ploidies. Copy number calls for non-mappable regions were imputed with neighboring copy number calls in confidently mapped regions, provided that the copy number on both sides of a non-mappable region were the same and the region was < 500 kb.

Assigning cell cycle state to scDNA-sequenced cells

For a given sample, we classified the genome of each sequenced cell $i \in I$ to one of three states (G0/G1, S, apoptotic) as follows. Under the assumption that the G0/G1 population is larger than any of the other populations, we defined the G0/G1 ploidy, p_{g0g1} , as the median ploidy across all sequenced cells of a given sample. We then calculate three features for each cell, x : i) its distance, d_x , to p_{g0g1} ; ii) its total number of breakpoints, b_x , and iii) the Pearson correlation coefficient, r_x , between the number of rare breakpoints observed in the cell per each chromosome and the number of replication origins per chromosome. Rare breakpoints were defined as breakpoints that were shared among less than 1% of cells.

We distinguished G0/G1 cells from cells with higher genome fragmentation. We divided cells into two groups – $P_A := \{x \in I \mid p_x \geq p_{g0g1}\}$ and $P_B := \{x \in I \mid p_x < p_{g0g1}\}$ – containing cells above and below the sample’s G0/G1 ploidy respectively. We fitted two sigmoid functions, one for each subgroup, to

model cell ploidy as function of the number of breakpoints per cell: $p_i \sim \begin{cases} f_A(b_i), & \text{if } i \in P_A \\ f_B(b_i), & \text{if } i \in P_B \end{cases}$

We then calculated $B := \operatorname{argmin}_b |f_A(b) - f_B(b)|$, as the threshold distinguishing G0/G1 cells from apoptotic cells:

$$\text{apoptotic} := \{x \in P_B \mid b_x \geq B\}$$

and from replicating cells:

$$S := \{x \in P_A \mid b_x \geq B\}$$

i.e. the yet unclassified cells were assigned to the G0/G1 state:

$$G0G1 := \{x \in I \mid b_x < B\} - \{S \cup \text{apoptotic}\}$$

The highest correlation to replication origins was observed for replicating cells (**Supplementary Fig. 5b-j**), supporting the accuracy of above cell cycle phase assignment strategy. We removed cell cycle specific breakpoints from further analysis, keeping only those breakpoints present among at least 1% of G0/G1 cells and encompassing segments of at least 5 Mb. Population-average copy number per segment per sample was calculated as the mean copy number across G0/G1 cells of that sample.

scRNA-Seq library preparation and sequencing

We used the Chromium Controller instrument (10X Genomics Inc., Pleasanton, CA) and the Single Cell 3' Reagent kit (v2) to prepare individually barcoded single cell RNA-Seq libraries following the manufacturer's standard protocol. Briefly, single cell suspensions were loaded on a Chromium Controller instrument and were partitioned in droplets. Reverse transcription is performed, followed by droplet breaking, and cDNA amplification. Each cDNA molecule thus contained the read 1 sequencing primer, a 16bp cell-identifying barcode, and a 10bp UMI sequence²⁰. We performed enzymatic fragmentation, end-repair, and a-tailing followed by ligation of a single-end adapter containing the read 2 priming site. PCR was performed using the Illumina P5 sequence and a sample barcode as described

earlier. Libraries were purified with SPRIselect beads (Beckman Coulter, Brea, CA) and size-selected to ~450bp. Finally, sequencing libraries were quantified by qPCR before sequencing on the Illumina platform using 26x98 paired-end reads. The Cellranger software suite was used to process scRNA data, sample demultiplexing, barcode processing, and single cell 3' gene counting. The cDNA insert, which is contained in the read 2, was aligned to the GRCh38 human reference genome. Cellranger provided a gene-by-cell matrix, which contains the read count distribution of each gene for each cell.

ScRNA-Seq data preprocessing

We used a curated set of seven biological and technical features to detect and remove low-quality cells^{20,34}. Biological features included: 1) transcriptome variance and expression of 2) cytoplasm localized genes, 3) mitochondrially localized genes, 4) mtDNA encoded genes. Technical features included: 5) % mapped reads, 6) % multi-mapped reads and 7) %non-exonic reads (intergenic & intronic). These features robustly identify low quality cells independently of cell type and of the experimental setting. The analysis was performed using “Celloline”³⁴ and the R-package “Cellity”³⁴. For additional processing, we used the software suite Seurat (v2.3.2)³⁵. Briefly, UMI counts were capped at the 99% quantile and only cells expressing at least 1,000 genes were included in subsequent analysis. Also, most cells classified by Cellity as low quality had a high percentage expressed mitochondrial genes as quantified by Seurat (**Supplementary Fig. 6**).

Assigning cell cycle state to scRNA-sequenced cells

Leveraging prior knowledge in form of cell-cycle annotated genes and deploying a rank-based comparison across single cells, has been shown to robustly capture the transcriptional cell-cycle signature across different cell types and experimental protocols²³. We employed such pathway-centric approach to classify the transcriptome of each sequenced cell to a cell cycle state as follows.

Quantification of cell cycle pathways activity: The gene membership of 39 cell cycle pathways was downloaded from the Reactome database³⁶ (v63), whereby each pathway consisted of at least ten genes (**Supplementary Table 4**). We used the GSVA method³⁷ to model variation in pathway activity across cells of a given cell line, as described in further detail below (**Methods** section 12).

Pathway and cell classification: Pathways were classified into three groups depending on their main activation timing during: i) G0/G1 (10 pathways, further referred to as P_{G0G1}); ii) S (5 pathways, further referred to as P_S) and iii) G2M (26 pathways, further referred to as P_{G2M}). Each class was normalized by its maximum activity across cells. As previously described, the 39 pathways were used as features to perform hierarchical clustering of cells (Euclidean distance metric and ward.D2 agglomeration method) into four clusters $C := \{C_1, C_2, C_3, C_4\}$. To classify each cluster $x \in C$ as either an G0/G1, S or G2M representative, we tested 39 null-hypotheses, one for each pathway p , namely that the activity of p in cells from x exceeds the activity of p in cells from $\{C - x\}$. We tested our hypotheses using the Wilcox rank-sum test and p-values were adjusted for multiple testing. For each pathway class $\delta \in \{G0G1, S, G2M\}$ we calculated the average effect size as:

$$P(x|\delta) := \frac{1}{|P_\delta|} \sum_{p \in P_\delta} e_{p,x}, \text{ where:}$$

$$e_{p,x} = \begin{cases} \text{effect size, if Wilcox } p \leq 0.05 \\ 0, \text{ otherwise} \end{cases}$$

Finally, we assigned cell cycle phase $\text{argmax}_{\delta \in \{G0G1, S, G2M\}} P(x|\delta)$ to each cluster $x \in C$.

LIAISON: Calling CNVs from scRNA-Seq

Linking single-cell genomes among contemporary subclone transcriptomes (LIAISON) is an approach to profile the CNV landscape of each scRNA-sequenced single cell of a given sample. The algorithm relies on two assumptions: i) a cell's average copy number state for a given genomic segment

influences the mean expression of genes within that segment across the same set of cells; and ii) the copy number variance of a given genomic segment across cells reflects the cells' expression heterogeneity for genes within that same segment (**Supplementary Fig. 3a,b**).

LIAYSON's algorithm involves the following: Let $x' \in \text{CN}$ be the measured copy number of a given cell-segment pair, and x its corresponding true copy number state. The probability of assigning copy number x to a cell i at locus j depends on: a) cell i 's read count at locus j and b) cell i 's read count at other loci, i.e. how similar the cell is to other cells that have copy number x at locus j . For (a), we fit a Gaussian kernel on the read counts at locus j across cells to identify the major and the minor copy number states of j as the highest and second highest peak of the fit respectively (**Supplementary Methods**). For (b), we use Apriori³⁸ – an algorithm for association rule mining – to find groups of loci that tend to have correlated copy number states across cells (**Supplementary Methods**). LIAYSON is implemented in R and is available on CRAN.

Identification of coexisting clones from scDNA-Seq or scRNA-Seq

Let CNF be the matrix of copy number states per non-private segment per G0/G1 cell, derived either from scRNA- or from scDNA-Seq, with entries (i, j) pointing to the copy number state of cell i for segment j . Pairwise distances between cells were calculated in Hamming space³⁹ of their segmental copy number profiles (rows in CNF), weighted by segment length. We used the BIONJ algorithm²⁵ to reconstruct a phylogenetic tree of G0/G1 cells from the distance matrix. A subtree was defined as a clone if the maximum distance between its cell members was less than 20% of the genome. Finally, we used the Pearson Correlation Coefficient calculated across segments to assign S and G2M cells to the clones detected among the G0/G1 population. The copy number profile of each detected subclone was calculated as the average profiles of assigned subclone members.

Integration of scRNA-Seq- and scDNA-Seq derived clones

Let R and D be the scRNA- and scDNA-Seq derived clone-by-segment matrices of copy number states.

Furthermore, let $S := S_R \cap S_D$, where S_R and S_D are the segments defining the columns of R and D respectively. We defined $X := R_S \cup D_S$ which was the union of scRNA-Seq and scDNA-Seq derived clones at overlapping genomic locations. We used the same hierarchical clustering procedure as above, only this time clones rather than cells were arranged into the resulting dendrogram T. We iterated through all binary subtrees $t \in T$ and assigned clones within t as:

- i) True positives (TPs) – t contains both, an scRNA- and an scDNA-clone
- ii) False positives (FPs) – t contains two scRNA-clones
- iii) False negatives (FNs) – t contains two scDNA-clones.

To validate scDNA-Seq derived clone detection, we used the same procedure, except the roles of FPs and FNs were flipped. Clones comprising less than 4% cells, which were not confirmed by both techniques, were excluded from further analysis.

Inferring clonal dynamics from distribution of replicating cells among clones

For each detected and confirmed clone of a given sample, we calculated whether its % replicating cell assignment was different than expected by chance from its G0/G1 representation. Hereby we excluded clones below 4% size, because their absolute cell count was too small to reliably perform these calculations. To infer positive selection, we used the hypergeometric distribution and calculated the p-value of sampling at least the observed number of replicating clone members, q , as:

$$P = \text{phyper}(q, m, n, k)$$

where k is the total number of cells sampled from the clone, n is the number of clone members in G0/G1 and m is the expected number of clone members that are replicating (assuming proportionality

to G0/G1 clone size). The p-value of sampling maximum q replicating cells was calculated by subtracting above value from 1, and was used to infer negative selection. P-values were adjusted for multiple hypotheses testing using the FDR method (R function “`p.adjust`”).

Pathway quantification

The gene membership of 1,417 pathways was downloaded from the Reactome database³⁶ (v63). First the transcriptome profiles of high quality cells detected within a given sample were scaled to the number of UMIs per cell (Seurat function “`ScaleData`”). We used the GSVA function³⁷ to model variation in pathway activity across cells of the sample (R function “`gsva`”, `mx.diff=TRUE`). GSVA starts by evaluating the expression magnitude of a given gene in a given cell, in the context of the sample population distribution. To reduce gene specific biases (i.e. caused by GC content and gene length), an expression-level statistic was calculated for each gene from a kernel estimation of its cumulative density function. GSVA then calculated a rank-based, cell specific enrichment scores using the Kolmogorov-Smirnov like random walk statistic. For any given sample, pathways for which less than ten gene members were expressed in the scRNA-Seq data were not quantified.

Assigning scRNA-sequenced single cells to cell types in P5931

We employed the method of Macosko *et al.*⁴⁰ to rank genes based on their normalized dispersion (Seurat^{35,41} function `FindVariableGenes`). We used 1,097 highly-variable genes to compute 60 principal components (Seurat function `RunPCA`). The first 51 principal components explained >90% of the variance in the data and were used as input for the subsequent tSNE analysis (Seurat function `RunTSNE`).

REFERENCES

1. Casasent, A.K., et al. Multiclonal Invasion in Breast Tumors Identified by Topographic Single Cell Sequencing. *Cell* **172**, 205-217.e212 (2018).
2. Gao, R., et al. Punctuated copy number evolution and clonal stasis in triple-negative breast cancer. *Nature genetics* **48**, 1119-1130 (2016).
3. Kim, C., et al. Chemoresistance evolution in triple-negative breast cancer delineated by single-cell sequencing. *Cell* **173**, 879-893.e813 (2018).
4. Wang, Y., et al. Clonal evolution in breast cancer revealed by single nucleus genome sequencing. *Nature* **512**, 155-160 (2014).
5. Morrissey, A.S., et al. Divergent clonal selection dominates medulloblastoma at recurrence. *Nature* **529**, 351-357 (2016).
6. Johnson, B.E., et al. Mutational analysis reveals the origin and therapy-driven evolution of recurrent glioma. *Science* **343**, 189-193 (2014).
7. Gerlinger, M. Metastasis Seeding Cells: Lone Invaders or Mass Migrators? *Clinical cancer research : an official journal of the American Association for Cancer Research* **24**, 2032-2034 (2018).
8. Turajlic, S., et al. Tracking cancer evolution reveals constrained routes to metastases: TRACERx Renal. *Cell* **173**, 581-594.e512 (2018).
9. Ben-David, U., et al. Patient-derived xenografts undergo mouse-specific tumor evolution. *Nature genetics* **49**, 1567-1575 (2017).
10. Ben-David, U., et al. Genetic and transcriptional evolution alters cancer cell line drug response. *Nature* **560**, 325-330 (2018).
11. Garvin, T., et al. Interactive analysis and assessment of single-cell copy-number variations. *Nat Methods* **12**, 1058-1060 (2015).
12. Zahn, H., et al. Scalable whole-genome single-cell library preparation without preamplification. *Nat Methods* **14**, 167-173 (2017).

13. Vitak, S.A., et al. Sequencing thousands of single-cell genomes with combinatorial indexing. *Nat Methods* **14**, 302-308 (2017).
14. Lan, F., Demaree, B., Ahmed, N. & Abate, A.R. Single-cell genome sequencing at ultra-high-throughput with microfluidic droplet barcoding. *Nat Biotechnol* **35**, 640-646 (2017).
15. Wang, L.Y., et al. Integrated sequencing of exome and mRNA of large-sized single cells. *Sci Rep* **8**, 384 (2018).
16. Macaulay, I.C., et al. G&T-seq: parallel sequencing of single-cell genomes and transcriptomes. *Nat Methods* **12**, 519-522 (2015).
17. Dey, S.S., Kester, L., Spanjaard, B., Bienko, M. & van Oudenaarden, A. Integrated genome and transcriptome sequencing of the same cell. *Nat Biotechnol* **33**, 285-289 (2015).
18. Patel, A.P., et al. Single-cell RNA-seq highlights intratumoral heterogeneity in primary glioblastoma. *Science* **344**, 1396-1401 (2014).
19. Zheng, G.X., et al. Haplotyping germline and cancer genomes with high-throughput linked-read sequencing. *Nat Biotechnol* **34**, 303-311 (2016).
20. Zheng, G.X., et al. Massively parallel digital transcriptional profiling of single cells. *Nat Commun* **8**, 14049 (2017).
21. Chen, C., et al. Single-cell whole-genome analyses by Linear Amplification via Transposon Insertion (LIANTI). *Science* **356**, 189-194 (2017).
22. Langley, A.R., Gräf, S., Smith, J.C. & Krude, T. Genome-wide identification and characterisation of human DNA replication origins by initiation site sequencing (ini-seq). *Nucleic Acids Res* **44**, 10230-10247 (2016).
23. Scialdone, A., et al. Computational assignment of cell-cycle stage from single-cell transcriptome data. *Methods* **85**, 54-61 (2015).
24. Croft, D., et al. The Reactome pathway knowledgebase. *Nucleic Acids Res* **42**, D472-477 (2014).
25. Gascuel, O. BIONJ: an improved version of the NJ algorithm based on a simple model of sequence data. *Molecular Biology and Evolution* **14**, 685-695 (1997).

26. Fehrmann, R.S., et al. Gene expression analysis identifies global gene dosage sensitivity in cancer. *Nature genetics* **47**, 115-125 (2015).
27. Fan, J., et al. Linking transcriptional and genetic tumor heterogeneity through allele analysis of single-cell RNA-seq data. *Genome research* **28**, 1217-1227 (2018).
28. Cancer Genome Atlas Research, N. Comprehensive molecular characterization of gastric adenocarcinoma. *Nature* **513**, 202-209 (2014).
29. Roschke, A.V., et al. Karyotypic complexity of the NCI-60 drug-screening panel. *Cancer Res* **63**, 8634-8647 (2003).
30. Khatri, B.S. Quantifying evolutionary dynamics from variant-frequency time series. *Sci Rep* **6**, 32497 (2016).
31. Nené, N.R., Dunham, A.S. & Illingworth, C.J.R. Inferring Fitness Effects from Time-Resolved Sequence Data with a Delay-Deterministic Model. *Genetics* **209**, 255-264 (2018).
32. Dayarian, A. & Shraiman, B.I. How to infer relative fitness from a sample of genomic sequences. *Genetics* **197**, 913-923 (2014).
33. O'Fallon, B.D., Seger, J. & Adler, F.R. A Continuous-State Coalescent and the Impact of Weak Selection on the Structure of Gene Genealogies. *Molecular Biology and Evolution* **27**, 1162-1172 (2010).
34. Ilicic, T., et al. Classification of low quality cells from single-cell RNA-seq data. *Genome biology* **17**, 29 (2016).
35. Butler, A., Hoffman, P., Smibert, P., Papalexi, E. & Satija, R. Integrating single-cell transcriptomic data across different conditions, technologies, and species. *Nat Biotechnol* **36**, 411-420 (2018).
36. Fabregat, A., et al. The Reactome Pathway Knowledgebase. *Nucleic Acids Res* **46**, D649-d655 (2018).
37. Hanzelmann, S., Castelo, R. & Guinney, J. GSVA: gene set variation analysis for microarray and RNA-seq data. *BMC Bioinformatics* **14**, 7 (2013).
38. Borgelt, C. & Kruse, R. Induction of Association Rules: Apriori Implementation.

39. Molparia, B., Nichani, E. & Torkamani, A. Assessment of circulating copy number variant detection for cancer screening. *PLoS one* **12**, e0180647 (2017).
40. Macosko, E.Z., et al. Highly Parallel Genome-wide Expression Profiling of Individual Cells Using Nanoliter Droplets. *Cell* **161**, 1202-1214 (2015).
41. Satija, R., Farrell, J.A., Gennert, D., Schier, A.F. & Regev, A. Spatial reconstruction of single-cell gene expression data. *Nat Biotechnol* **33**, 495-502 (2015).

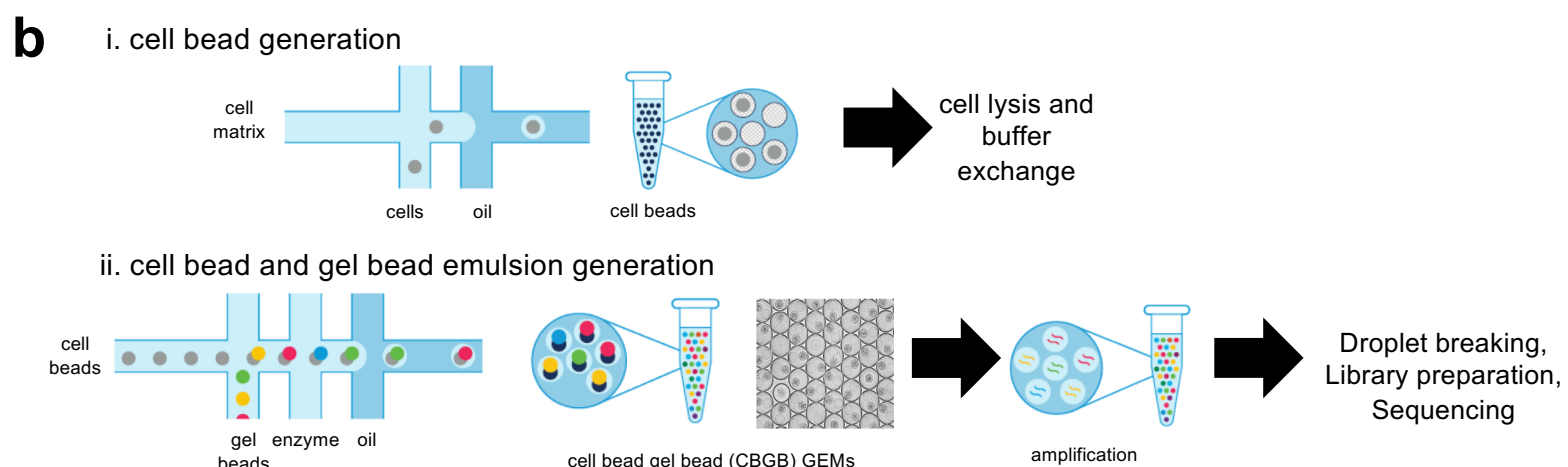
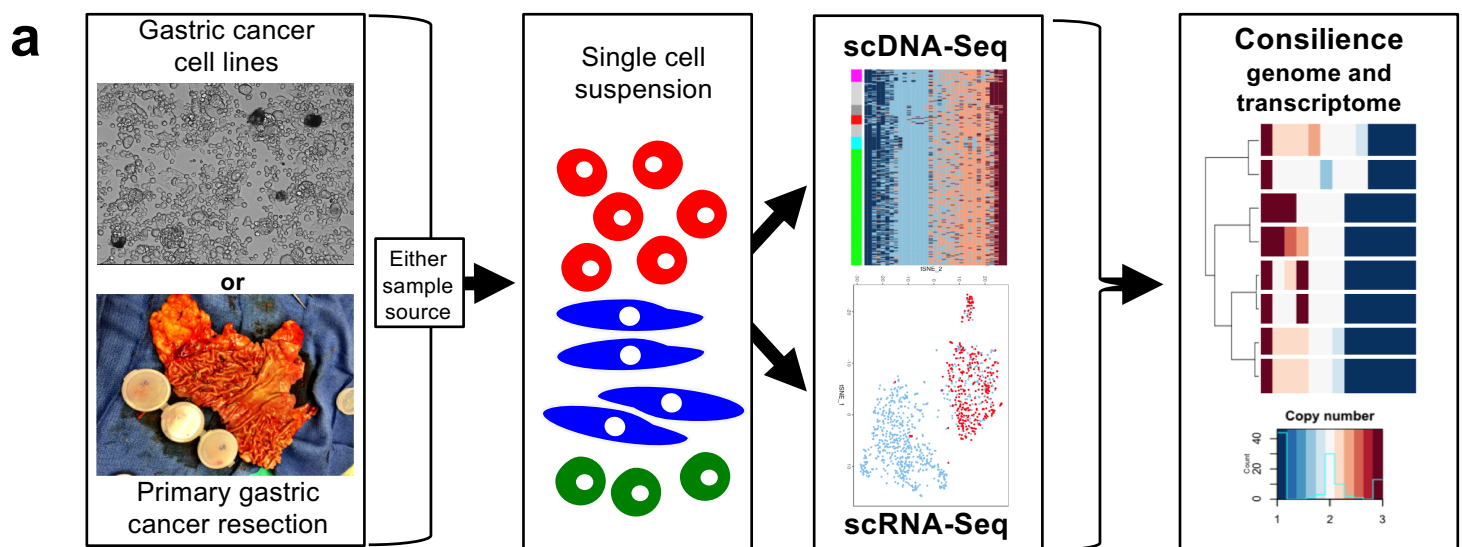


Figure 1

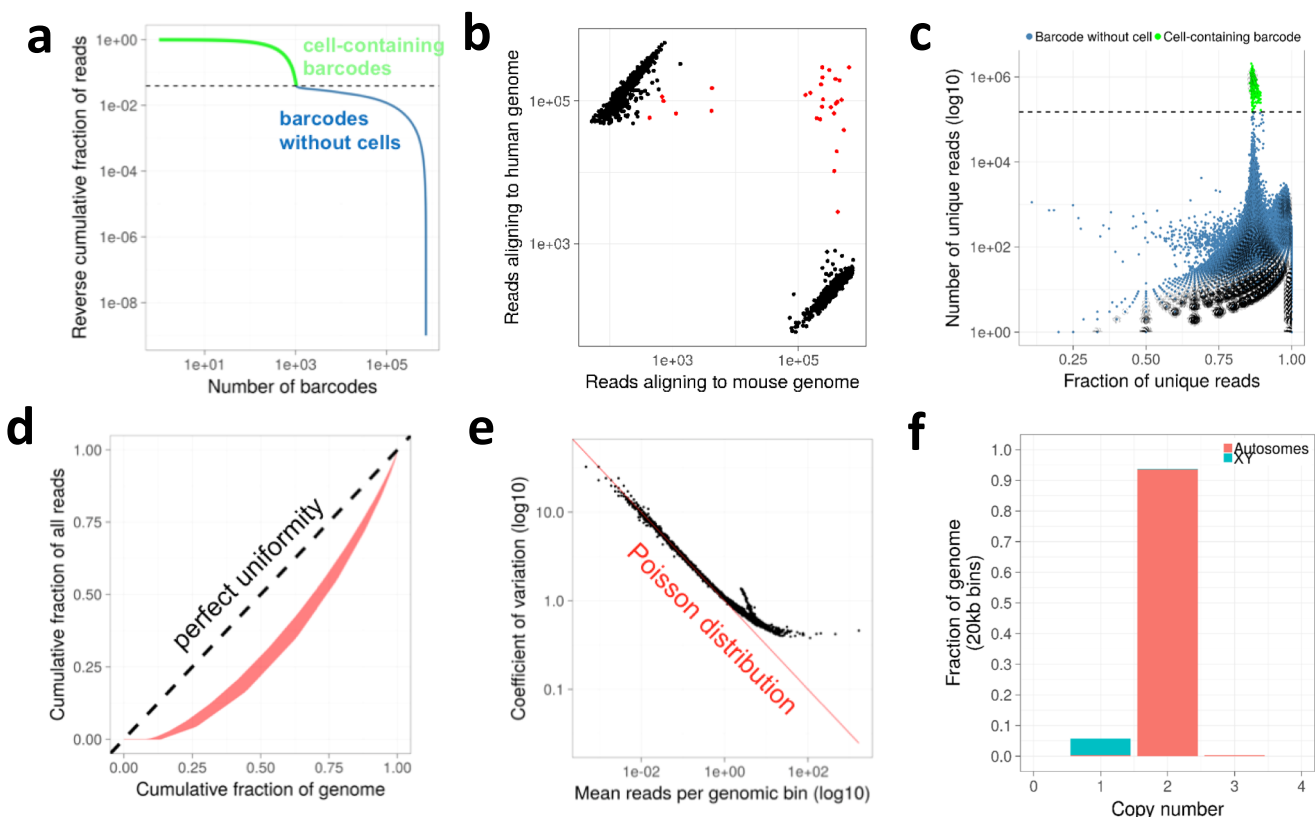


Figure 2

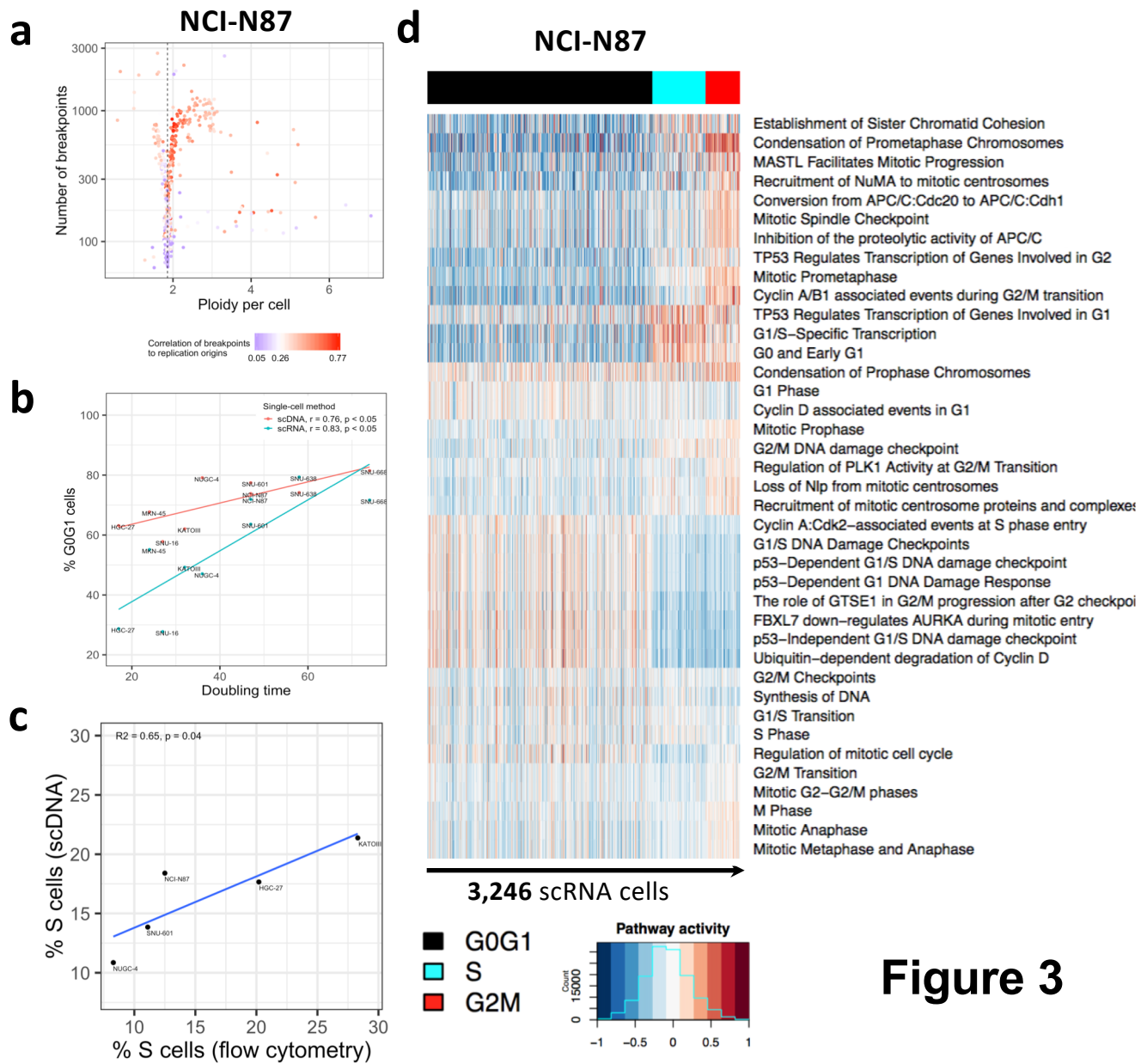


Figure 3

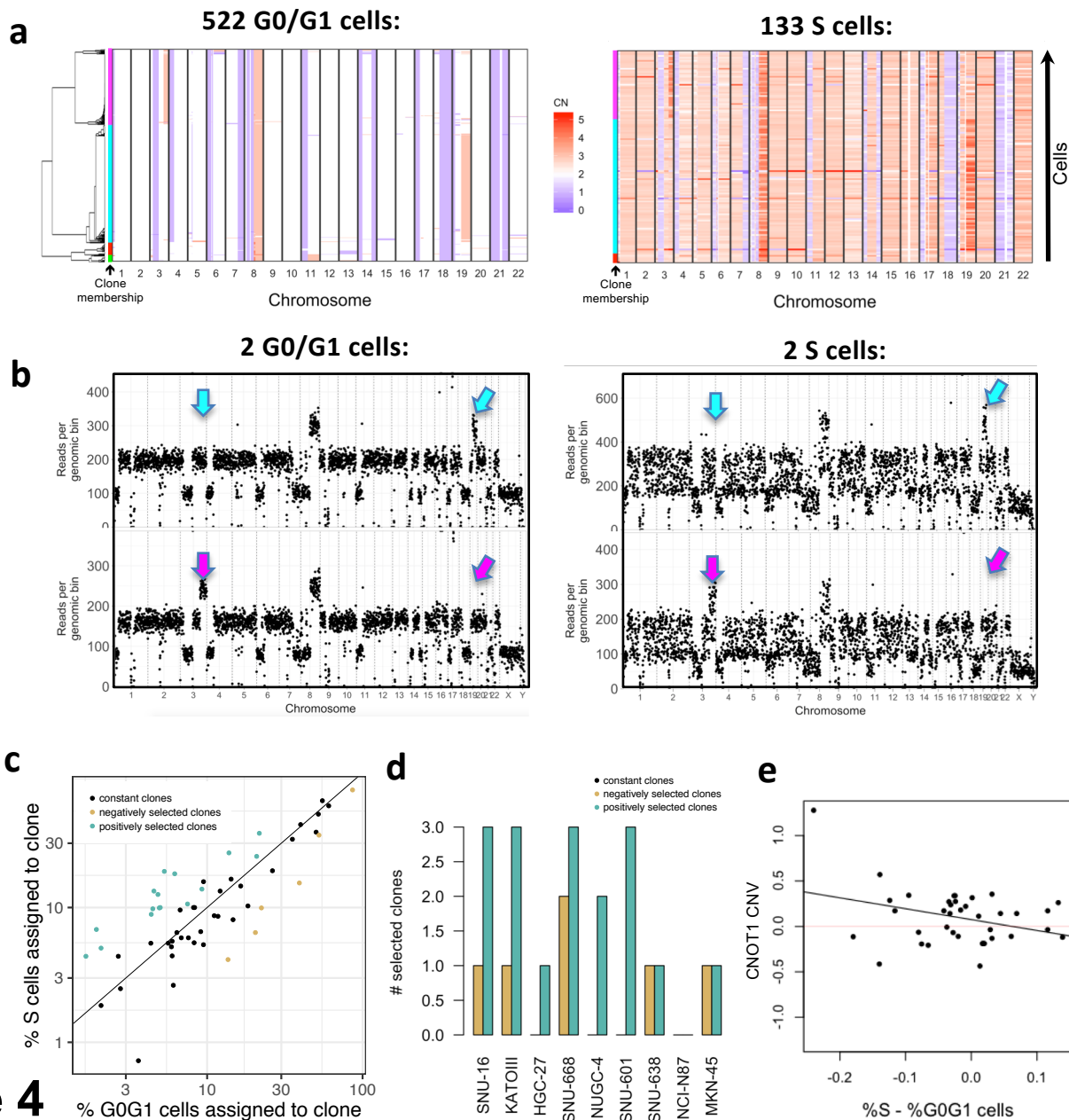


Figure 4

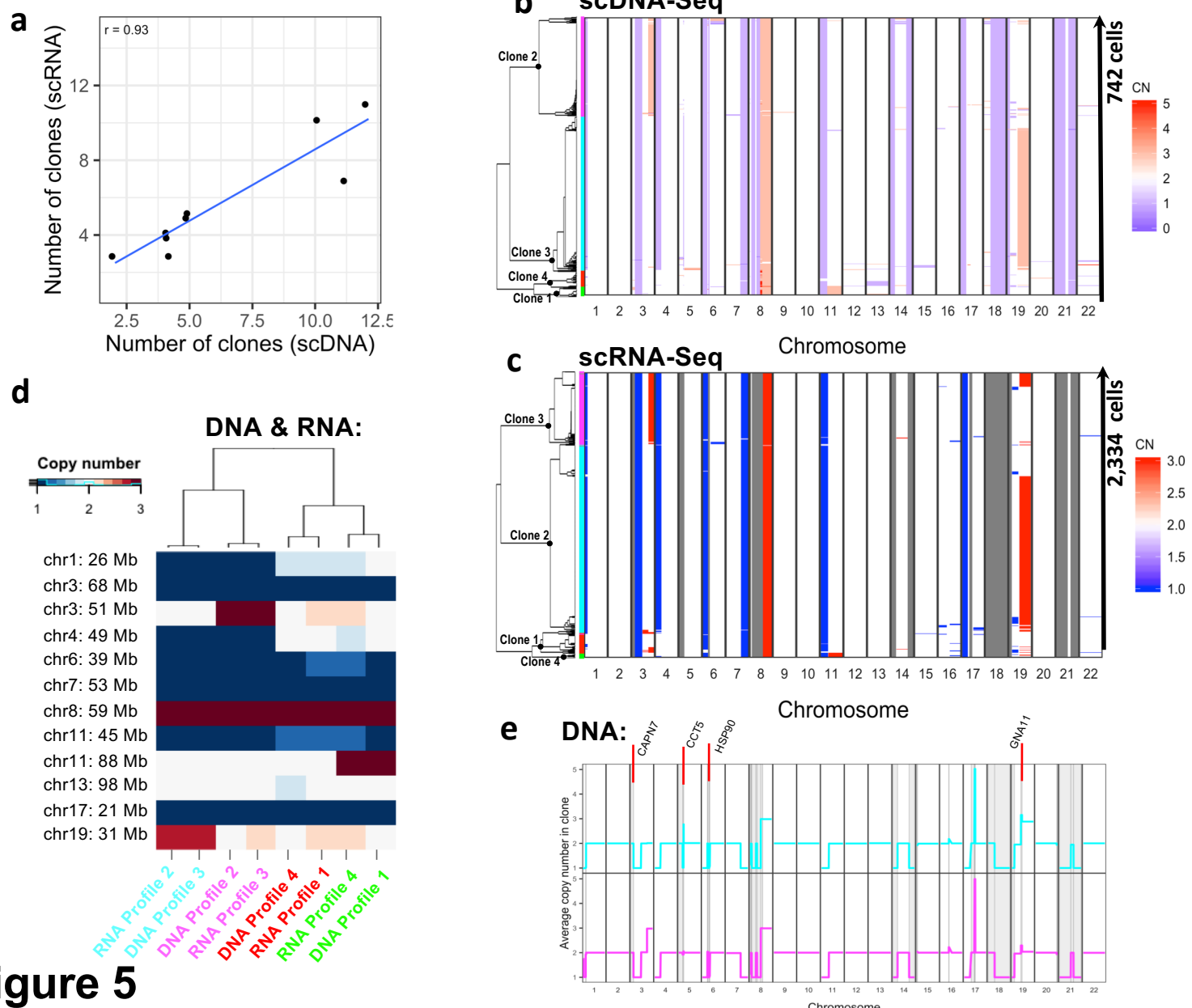
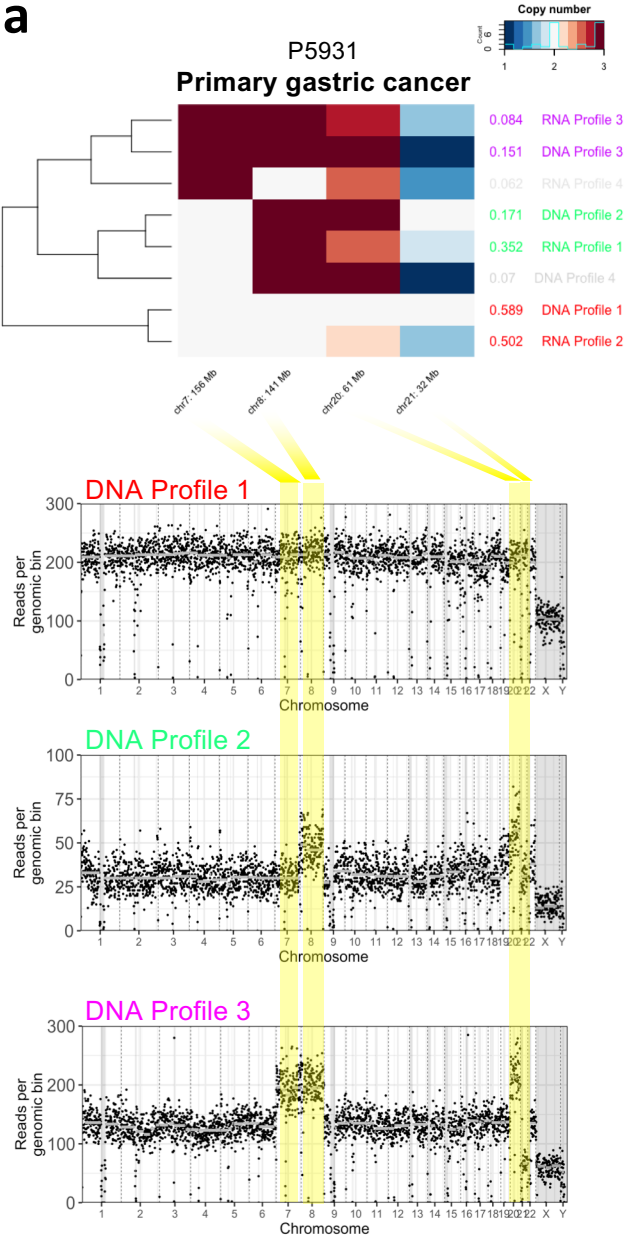
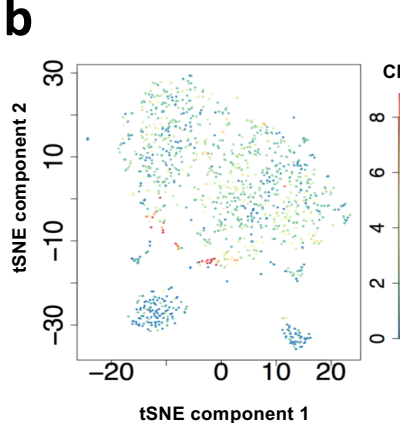


Figure 5

a



b



c

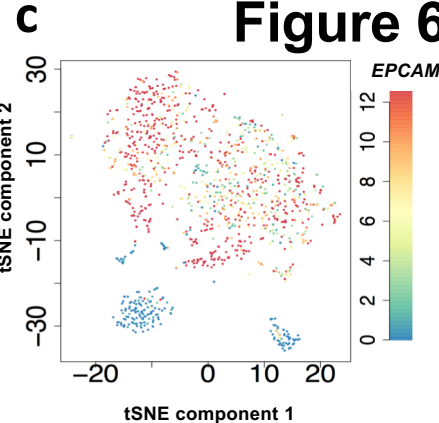
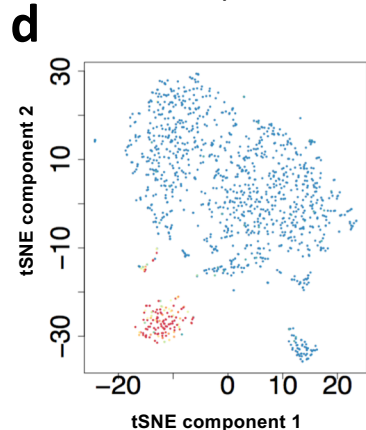
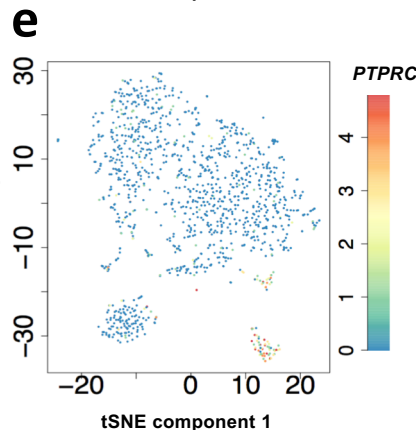


Figure 6

d



e



f

